Posiva SKB Report 02
September 2017

Evaluation of a gas shield for friction stir welding of copper canisters

Matts Björck
Henri Pehkonen
Leena Vuori
Mikael Tigerström
Kimmo Lahtonen
Mika Valden
Tero Purhonen
Lars Cederqvist

POSIVA OY

Olkiluoto
FI-27160 Eurajoki, Finland
Phone +358 2 837 231
posiva.fi

SVENSK KÄRNBRÄNSLEHANTERING AB

SWEDISH NUCLEAR FUEL
AND WASTE MANAGEMENT CO

Box 3091, SE-169 03 Solna
Phone +46 8 459 84 00
skb.se

ISSN 2489-2742
Posiva SKB Report 02
SKB ID 1525933
Posiva ID RDOC-104825
September 2017

Evaluation of a gas shield for friction stir welding of copper canisters

Matts Björck, Mikael Tigerström, Lars Cederqvist
Svensk Kärnbränslehantering AB

Henri Pehkonen, Maskinteknik AB

Leena Vuori, Kimmo Lahtonen, Mika Valden
SurfLab Solution Oy

Tero Purhonen, Posiva Oy

Keywords: Friction stir welding, FSW, Oxide particles, Copper oxide, Gas shield, Hydrogen embrittlement.

A pdf version of this document can be downloaded from www.skb.se or www.posiva.fi.

Abstract

Friction Stir Welding (FSW) has been selected by Svensk Kärnbränslehantering AB and Posiva Oy as the reference technique for sealing the copper canister used in the KBS-3 method. When FSW is conducted in air, oxides will form on the joint surfaces and will disperse and become embedded in the weld. This causes elevated levels of oxygen in the weld. The work presented in this report details an optimisation of the equipment and process to lower the oxygen content in the weld. The study was conducted on a full-scale welding machine installed at the Canister Laboratory in Oskarshamn, Sweden.

The FSW machine was retrofitted with a gas-shielding shroud that covered the entire joint line throughout the welding sequence. The gas shield was characterised by measuring the oxygen content at the joint line of the canister with a custom-designed weld. The oxygen content in the gas shield was determined to be less than 50 at-ppm.

Oxides and dirt can be present at the joint surfaces before welding; therefore, five different cleaning methods were compared: abrasive cleaning, laser cleaning, CO_2 cleaning, plasma cleaning and stainless steel brush cleaning. Of these methods, the abrasive cleaning method was found to be the most suitable for the development work due to its low oxide layer thickness and simple usage.

The final evaluation of the gas shield was conducted by producing three full-size welds. The first weld had a shielding gas, Ar, on the outside of the joint line. In addition to the external shielding gas, the second weld had an inert atmosphere, N_2, on the inside (root side) of the joint line. The last weld was a variant of the second weld with 2 at-% H_2 mixed into the gases. The welds were evaluated by measuring the oxygen content and by conducting hydrogen annealing tests according to ASTM B577-16 at two cross sections per weld. In addition, the oxide amount was evaluated by inspecting weld cross sections metallographically.

The results showed that all sampled positions had oxygen content below 3 wt-ppm, which was below the upper limit of 5 wt-ppm for the base material. The hydrogen annealing tests were evaluated using a comparison chart for copper oxide specified in ASTM F68-10. All welds where determined to have a copper oxide level of 1/C, which is the lowest level on the chart. Consequently, these welds can be considered as unsusceptible to hydrogen embrittlement. The metallographic inspection revealed that the oxide particles content was reduced in welds with an internal shielding gas, primarily around the start position.

Sammanfattning

Friktionsomrörningsvetsning (FSW, eng. Friction stir welding) har valts som referensmetod av Svensk Kärnbränslehantering AB och Posiva Oy för förslutning av kopparkapseln som skall användas i KBS-3 konceptet för slutförvar av använt kärnbräsle. När FSW utförs i luft bildas oxider på fogytorna dessa kommer att bli inbäddade i svetsgodset. Detta höjer syrenivån i materialet. Denna rapport beskriver utvecklingsarbetet med att minska syrehalten i svetsen. Arbetet utfördes vid Kapsellaboratoriet i Oskarshamn, Sverige.

För att förbättra processen byggdes ett nytt permanent gasskydd på FSW maskinen. Gasskyddet utformades så att det täckte hela foglinjen under alla sekvenser vid svetsning. Syrehalten i gas-skyddet uppmättes till att vara under 50 at-ppm med hjälp ett speciellt utformat svetsobjekt.

Oxider eller smuts kan även finnas på fogytorna innan svetsning. Därför undersöktes även 5 stycken rengöringsmetoder; slipning, laserrengöring, kolsyreisblästring, plasmarengöring och rengöring med rostfri stålborste. Av dessa metoder valdes slipning till de fortsatta studierna på grund av den låga oxidtjockleken samt det enkla handhavandet.

Den sista utvärderingen av gasskyddet gjordes genom tre fullvarvssvetsar. Den första svetsen hade skyddsgas, Ar, på utsidan av foglinjen, den andra hade skyddsgas, N_2, även på insidan. Den tredje svetsen hade samma konfiguration som den andra men med 2 at-% H_2 inblandat i skyddsgaserna. Resultatet utvärderades genom att mäta syrehalten i svetsen, utföra värmebehandling i vätgas-atmosfär enligt ASTM B577-16. Även metallografisk undersökning av ett flertal tvärsnitt gjordes med en metod utvecklad för att hitta små oxidpartiklar.

Utvärderingen visade att den högsta syrehalten var under 3 vikts-ppm vilket är under specifikationen för basmaterialet på 5 vikts-ppm. Värmebehandlingen i vätgasatmosfär jämfördes enligt skala från ASTM F68-10. Alla svetsar befanns ha en nivå 1/C vilket är den lägsta nivån. Följaktligen är svetsarna inte mottagliga för väteförsprödning. Den metallografiska undersökningen visade att svetsar utförda med intern skyddsgas hade, främst vid startpositionen, en lägre halt av oxidpartiklar.

Tiivistelmä

Posiva Oy ja Svensk Kärnbränslehantering AB ovat valinneet kitkatappihitsauksen (Friction Stir Welding, FSW) kuparikapselien sulkemistekniikaksi KBS-3-menetelmässä. Koska FSW tehdään ilmassa, liitospinnoille syntyy hitsaussaumaan leviäviä oksideja, mikä nostaa hitsin happipitoisuutta. Tässä raportissa käsitellään hitsauslaitteiston ja –menetelmän optimointia hitsaussauman happipitoisuuden alentamiseksi. Työ tehtiin täysimittaisella hitsauslaitteistolla Ruotsissa Oskarshamnin kapselointilaitoksella.

FSW-hitsauslaitteeseen jälkiasennettiin suojakaasuvaippa, joka kattoi koko liitossauman hitsauksen ajan. Kaasusuojaus tutkittiin mittaamalla happipitoisuus kapselin liitossaumaan kustomoiduista hitsistä. Suojakaasun happipitoisuus oli alle 50 at-ppm.

Ennen hitsausta, yhdistettävillä pinnoilla saattaa olla oksideja ja epäpuhtauksia. Tämän vuoksi verrattiin viittä puhdistusmenetelmää: abrasiivinen, laser-, CO_2-, plasma- ja terässharjapuhdistus. Näistä menetelmistä abrasiivisen puhdistuksen havaittiin soveltuvan parhaiten hitsaustesteihin ohuen oksidikerroksen ja helppokäyttöisyyden vuoksi.

Kaasusuojauksen lopullinen testaus suoritettiin valmistamalla kolme täysimittaista hitsiä. Ensimmäisessä suojakaasuna oli Ar liitoksen ulkopuolella. Ulkopuolisen suojakaasun lisäksi, toisessa hitsissä oli liitoksen sisäpuolella inertti N_2-atmosfääri. Viimeisessä hitsissä toisen hitsin suojakaasuihin lisättiin 2 at-% H_2:a. Hitsejä arvioitiin mittaamalla happipitoisuus ja testaamalla vetyhehkutusta ASTM B577-16-standardin mukaisesti hitsin kahdesta poikkileikkauksesta. Tämän lisäksi hapen määrä arvioitiin tutkimalla hitsin poikkileikkauksia metallografisesti.

Tulokset osoittavat, että kaikkien näytteiden happipitoisuus oli alle 3 wt-ppm, joka on alle perusmateriaalin ylärajan 5 wt-ppm. Vetyhehkutustestejä arvioitiin käyttämällä ASTM F68-10 -standardin mukaista kuparioksidien vertailutaulukkoa. Kaikkien hitsien kuparioksidipitoisuus oli alle 1/C -tason, mikä on taulukon alhaisin arvo. Tämän perusteella tutkitut hitsit eivät ole alttiita vetyhaurastumiselle. Metallografisen tutkimuksen perusteella oksidipartikkelipitoisuus väheni hitseissä, joissa oli sisäinen kaasusuojaus, erityisesti hitsin aloituskohdan ympärillä.

Contents

1 Introduction

The spent nuclear fuel from nuclear power plants in Sweden and Finland is intended to be deposited, using the KBS-3 method, in the bedrock at a depth of 500 m. The fuel is placed in copper canisters supported internally by a load-bearing nodular cast iron insert. The copper canister functions primarily as a corrosion barrier that isolates the nuclear fuel from the surroundings. The canister itself is surrounded by bentonite clay that acts as a diffusion barrier and as a cushion against rock movements. The system is intended to isolate the radioactive fuel from the biosphere for more than 100 000 years, which places stringent demands on all components. The copper shell is proposed to be manufactured from ingots of oxygen-free electronic copper grades Cu-OFE or Cu-OF1 with the following additional requirements: O < 5 wt-ppm, P 30–100 wt-ppm, H < 0.6 wt-ppm, S < 8 wt-ppm (SKB 2010).

Friction Stir Welding has been selected by SKB and Posiva as the reference welding technique for the sealing of the copper shell. Cederqvist (2014) and Purhonen (2014) detailed the welding procedure and the development work. The two reviews showed that the developed FSW processes are capable of producing welds that fulfil the criteria for mechanical and corrosion properties.

However, welds, primarily those produced in air, can contain streaks of oxide particles. These oxides can originate from the joint surfaces prior to welding or can be produced due to the high temperatures that the joint surfaces are exposed to prior to joining (Savolainen 2012). The amount of oxides formed during welding has been investigated experimentally (SKB 2010, Cederqvist 2014), as well as modelled (Björck 2015) using a previously derived oxidation model for copper (Björck and Elger 2013).

Although the welds produced in air fulfil all the functional requirements (SKB 2010), a reduction in the oxide particles has been attempted to optimise the welding method. This improvement is desired because there have been some indication that rupture can occur close to the line of oxide particles (Savolainen 2012). It is also known from FSW of aluminium that oxide particles in the weld can cause a reduction in the mechanical strength (Chen et al. 2006, Zhou et al. 2006). A large amount of oxide particles has also been shown to be detrimental to the mechanical integrity of copper FSW welds (Rantala et al. 2015). These reports indicate that oxide particles formed during welding might affect the ductility of the weld material. Additionally, from a long-term safety perspective, it is desirable to have a weld material that is as similar as possible to the base material.

One method to reduce the amount of oxide particles in the weld is to reduce the oxygen content in the environment surrounding the weld area with a gas shield of an inert gas. The FSW machine at the Canister Laboratory was initially installed without a gas shielding system. This work reports the construction and evaluation of a gas shielding system for the aforementioned FSW machine. In order to ascertain that the effect of the gas shield are evaluated the cleaning procedure is optimised on a lab scale by comparing several different industrially applicable methods with X-ray photoelectron spectroscopy (XPS). The evaluation of the gas shield is performed using full circumferential welds with different gas shielding configurations, which are analysed regarding the amount of oxide particles and the oxygen content in the welds.

2 Gas shield

2.1 Design and construction

The description of the gas shield design can be found in Pehkonen's (2014) Master thesis. The chosen design is based on the experience gathered from the previous gas shields. The most important design criteria are protecting the entire joint line during the welding process, free of any gaps, without restricting the welding head.

Figure 2-1 shows an overview of the welding system. The polymethyl methacrylate (PMMA) panels that comprise the gas shield are marked in yellow. There are four panels in total, and they are supported by the steel frame around the welding head or by brackets. On the upper side, the panels create a seal against a collar on the cooling clamp. The cooling clamp was rebuilt into a single piece to provide a gas barrier and a more uniform pressure on the canister's lid. On the lower side, the panels create a seal against a steel ring that houses a radially inflatable silicon rubber seal that provides a seal against the canister. All seals against the PMMA panel are composed of silicon rubber. A steel plate with mounting holes and feedthroughs is placed behind the welding head so that different sensors can be inserted close to the tool (Figure 2-2). This steel plate is connected to a rubber bellow that allows the welding head to move in vertical and radial directions, which is necessary for the welding sequence. A picture of the gas shield during welding is shown in Figure 2-3.

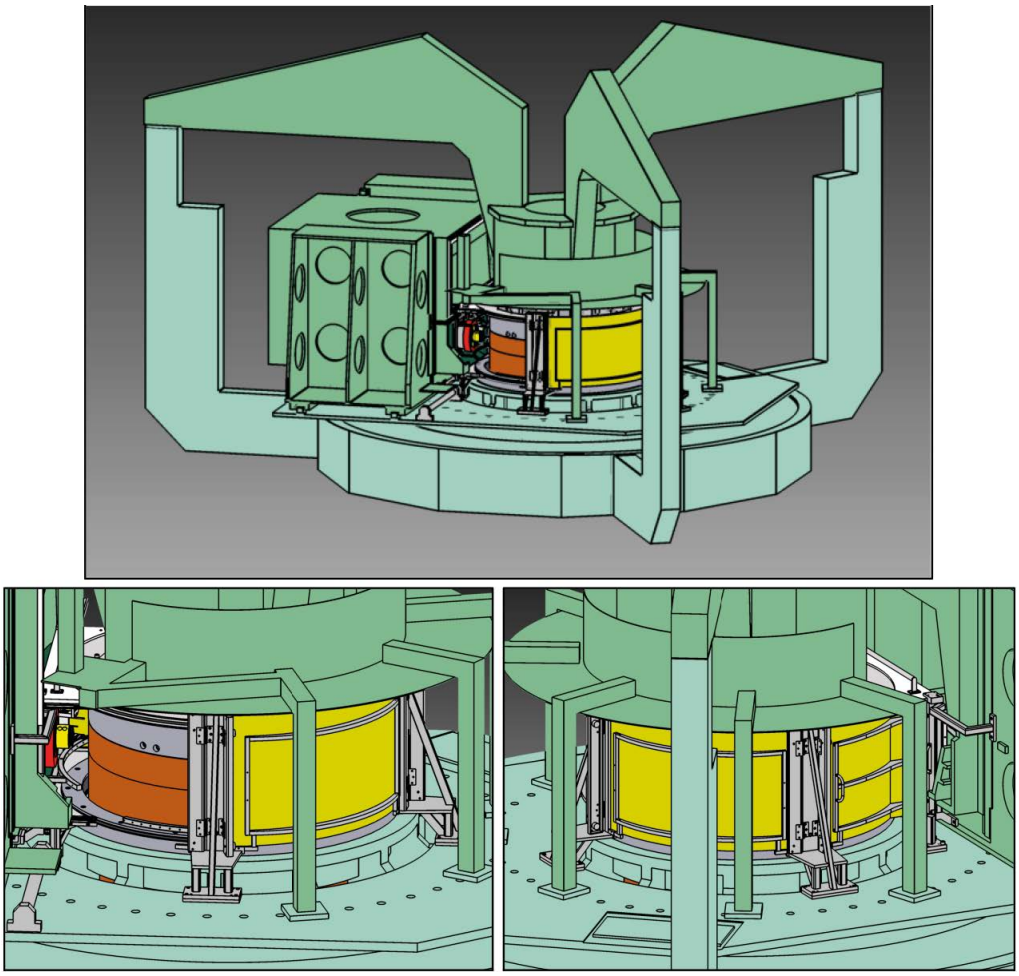

Figure 2-1. *An overview of the welding machine with PMMA shields surrounding the weld in yellow. One shield is removed in the drawings to show the welding head and the tool. The lower sketches show a detailed view of the layout of the gas shield. The lower right picture shows the backside relative to the other two pictures.*

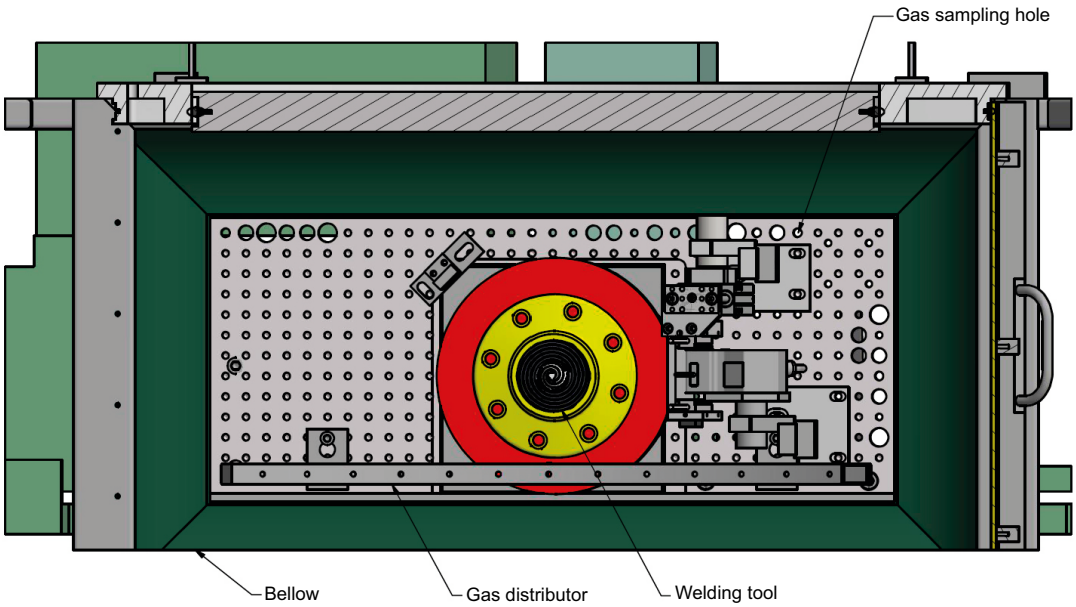

Figure 2-2. *A front view of the welding head with a steel plate with threaded holes behind it. Different depth sensors and gas distributor 0 is mounted on the steel plate. The bellow allows motion in the plane of view as well as out of plane. The larger holes are used as feedthroughs for cables and gas lines.*

Figure 2-3. *The gas shield during welding. To the right, the supporting bracket can be seen. The white lines on the upper and lower part of the PMMA panels are seals.*

During welding, the oxygen content in the gas shield is monitored at four different locations: at the welding head and at each of the three brackets that holds the PMMA shields (Figure 2-1 and Figure 2-4). At the welding head, the oxygen level is continuously monitored with a Rapidox 1100 ZF through a hole on the experimental board, see Figure 2-2. At the three remaining positions, the oxygen content is monitored with a Rapidox 1100 ZR3 meter. These sampling points are located on the brackets supporting the PMMA shields located in the middle of the gas distributors (Figure 2-4) and are positioned at the same height as the joint line. The Rapidox 1100 ZR3 multiplexes sequentially between the different positions every minute. The gas is extracted from the gas shield with a sampling pump. Both oxygen meters are incorporated into the Programmable Logic Controller (PLC) software, and the readings are collected simultaneously with the other welding parameters.

2.2 Oxygen content in the gas shield

To characterise the gas shield, an old weld was prepared with a sampling hole (Figure 2-5). A Rapidox 1100 ZF (measurement range: 0.1 at-ppm–21 at-%) instrument was connected to the sampling hole, and the oxygen level was collected using an NI USB-6001 14-bit DAQ (measurement range ±10 V, absolute accuracy 26 mV) connected to a computer. After filling the gas shield with argon the machine was moved so all positions along the joint line were sampled.

The recorded oxygen content around the gas shield can be seen in Figure 2-6. The oxygen content was < 50 at-ppm at all positions. The higher oxygen level around the weld head could be due to the larger volume of the gas shield at that position along with a more complicated geometry of the seals around the welding head.

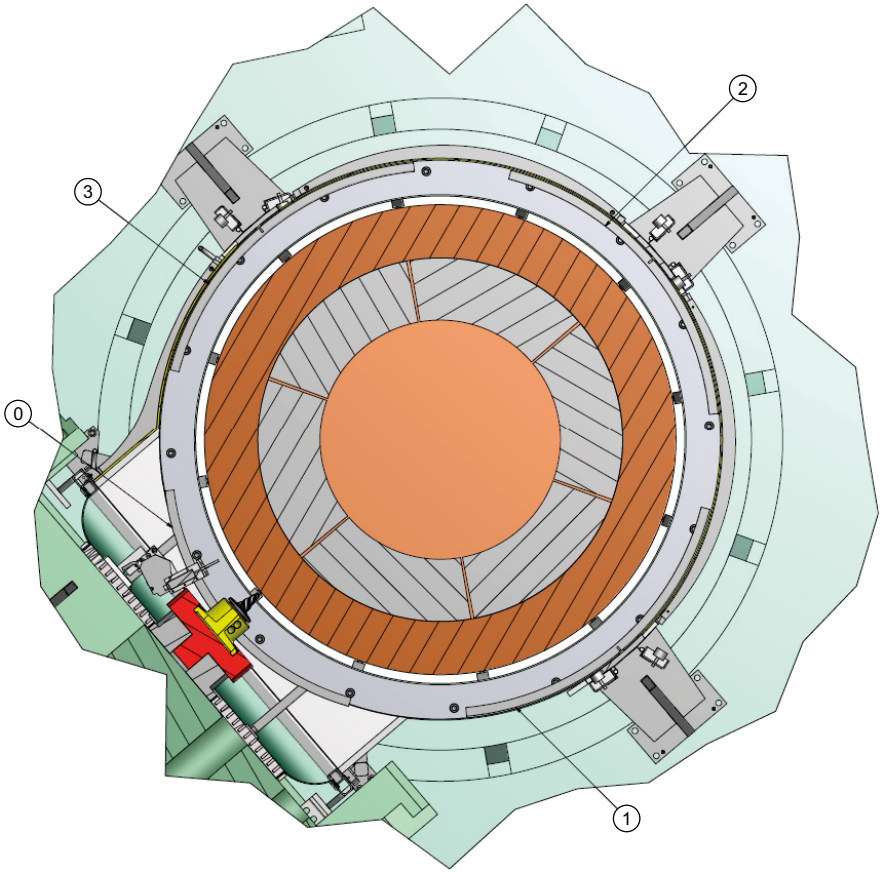

Figure 2-4. *A cut-away view of the gas shield from above showing the placement of the gas distributors. The numbers refer to the numbering of the distributors throughout this report. Distributor 0 is located at the welding head, and the others are numbered counter clockwise from this position, as indicated in the diagram.*

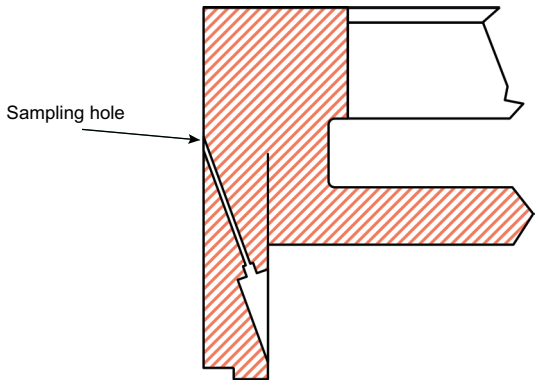

Figure 2-5. *A cut-away view of the lid used to characterise the gas shield. The sampling hole is located to the left.*

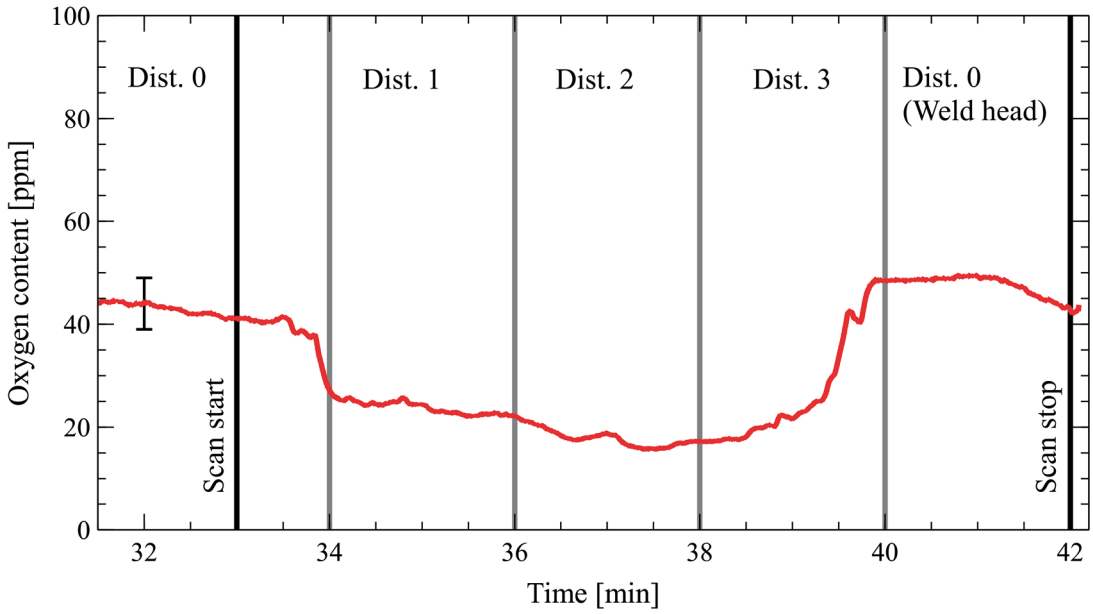

Figure 2-6. *The oxygen content in the gas shield as a function of time while moving the weld around the lid. The numbering of the distributors is defined in Figure 2-4. The estimated absolute accuracy (95 % confidence interval) of the measurement is shown with a single error bar in the figure.*

3 Investigation of joint line cleaning methods

A few minutes after a clean copper surface has been exposed to air, an oxide layer forms with a thickness of a few nm (Scheuerlein and Taborelli 2006). After this formation, the oxidation decelerates. Hydrocarbons from the surrounding air also deposit on the surface. Consequently, in a production-like environment, a completely clean copper surface is not practical. Therefore, the goal of cleaning the copper is to create a reproducible surface state that is acceptable for continued welding that removes residues from handling and previous production steps.

To determine a suitable cleaning method, a comparison of different methods was envisioned. Discussions were conducted between the author's companies, which resulted in a number of methods that could be used. Chemical methods, such as electrolytic polishing (Boman et al. 2014), were abandoned due to the perceived difficulties in implementation at the planned facilities on these large components. The resulting identified methods were abrasive cleaning using a 3M wheel, which is the method that has been historically used in weld development, CO_2 cleaning, laser cleaning and plasma cleaning. At a later stage, it was noted that cleaning with a stainless steel brush was recommended by the inital development at The Welding Institute (TWI) in the United Kingdom (Andrews 2004, pp 43–44). Consequently, cleaning with a rotating steel brush was also included in the study.

The methods were evaluated using X-ray photoelectron spectroscopy (XPS), which is a surface-sensitive technique in which an X-ray source excites electrons from the atoms that constitute the material. The electrons are energy analysed, and different elements and their chemical state can be identified by the kinetic energy of the electrons. The expelled electrons originate from a surface layer with a thickness of 2–10 nm. Further details about XPS can be found in the literature (Zangwill 1988).

3.1 Experimental details

The cleaning studies were performed by SurfLab Solutions Oy at the facilities of Surface Science Laboratory, Tampere University of Technology. Contact angle measurements were used as an initial test of the surface cleanliness. Different cleaning parameters were briefly tested for CO_2, plasma and laser cleaning methods, depending on the parameter set-up that resulted in the smallest contact angle. This parameter set-up was then used for each method to clean the samples that were selected for the XPS analysis. The samples were also imaged with an optical microscope.

3.1.1 Samples

Copper samples with dimensions of $10 \times 10 \times 2.8$ mm^3 were prepared by TH Tools Oy. The samples were numbered on the bottom; samples 17–26 were prepared with cutting fluids, whereas samples 1–16 and 27 were prepared without cutting fluids. The samples for stainless steel brush cleaning were numbered similarly and are indicated as #xN (N for new) to distinguish them from samples studied initially. The samples were stored in microtiter plates before and after cleaning and during ageing. Figure 3-1 shows an as-received sample attached to an XPS sample holder. Optical microscopy images show the grooved surface of the as-received samples. Some contamination particles are also visible on the sample prior to cleaning. Curved grooves were observed on all samples.

3.1.2 Reference samples

Three samples were used as references: as-received, sputter cleaned and air oxidized. The as-received sample (blown with N2 prior to the XPS experiments) represents the initial stage of the copper before cleaning. The unoxidized copper reference was prepared by sputtering the sample in ultra-high vacuum (UHV) with Ar+ ions. The sputtering removed the surface contamination and the oxide layer. To determine the effect of air exposure, the sputter-cleaned Cu sample was exposed to air for 15 min before evacuating the sample to UHV for XPS measurements. The exposure time was adjusted so that it was equal to the time required to load the cleaned samples and to begin evacuating the load lock of the XPS system.

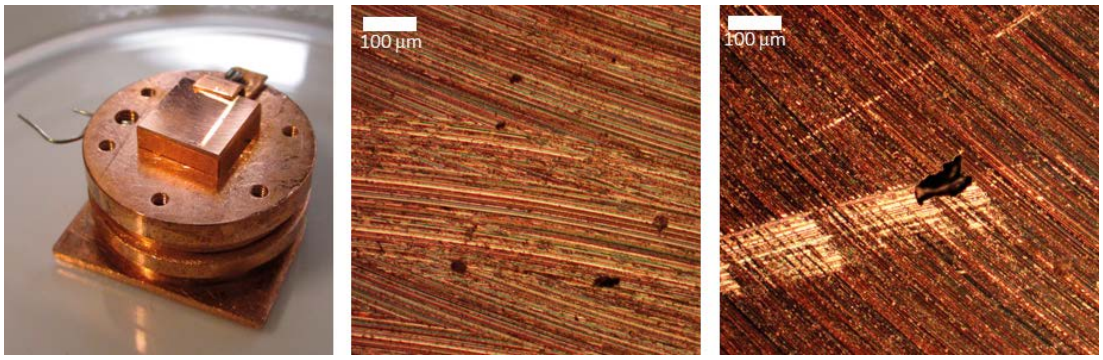

Figure 3-1. *Sample attached to XPS sample holder (left). Optical microscopy images of as-received samples (centre and right).*

3.1.3 Contact angle measurements

Contact angle measurements were performed as an initial test for surface cleanliness. A drop of deionized (DI) water was pipetted onto the sample surface; then, the sample was photographed. The contact angle is higher on hydrophobic surfaces and lower on hydrophilic surfaces.

The contact angle was determined from a photograph. The error of the determination of the angle was estimated as ± 5°. A 10 µl drop of deionized water was used for the measurements.

3.1.4 Abrasive cleaning

Abrasive cleaning was performed by pressing a grinding wheel (3M Scotch-Brite PF-ZS, ∅ 100 mm, z 45 mm, shaft 6 mm, part no. 07212 A. Very Fine) attached to a power drill (rotation speed about 600 rpm) on the sample in the jig for 15 s. The abrasive media in the griding wheel were Al_2O_3. The sample surface was then wiped with lint-free paper wetted with ethanol (EtOH), followed by rinsing with EtOH and drying with N_2. Mechanical cleaning removed material from the surface. The curved grooves observed on the as-received samples were removed. The contact angle varied between 53° (perpendicular to the grooves) and 58° (parallel to the grooves, Figure 3-2).

3.1.5 CO_2 cleaning

The CO_2 cleaning was performed by Arsalin Oy, which also provided the equipment. In the method, CO_2 ice granules are blown onto the copper surface using high-pressure air. The CO_2 ice sublimates at the surface, which cools to approximately −70 °C. The dirt particles are removed due to the rapid expansion of CO_2 ice to gas.

During the cleaning procedure, the cleaning time (1 min), nozzle size (5) and the CO_2 consumption (50 kg/h) were constant. The air pressure was varied between 8, 10 and 12 bar (air consumption 2.1, 2.6 and 3.0 m^3/min, respectively).

The contact angle was dependent on the air pressure used during cleaning. The smallest contact angle (50°) was obtained with 10 bar of air pressure. Both increasing and decreasing of the air pressure led to higher contact angles: 66° with 12 bar and 58° with 8 bar. Thus, the 10 bar air pressure was chosen for the samples prepared for XPS. The XPS samples were allowed to warm up for a few minutes after the cleaning procedure and then were removed from the jig. The condensed water on the sample was removed by blowing N_2 on the surface.

CO_2 cleaning alters the surface morphology. Figure 3-3 depicts the optical microscope images of CO_2 cleaned copper surfaces. The dents are caused by the collision of CO_2 granules on the surface.

3.1.6 Laser cleaning

Laser cleaning was performed by Meuro-Tech Oy using cleanLASER equipment. Powerful, very short, rapid and moving laser pulses produce micro-plasma bursts, shockwaves and thermal pressure, resulting in sublimation and ejection of the target material.

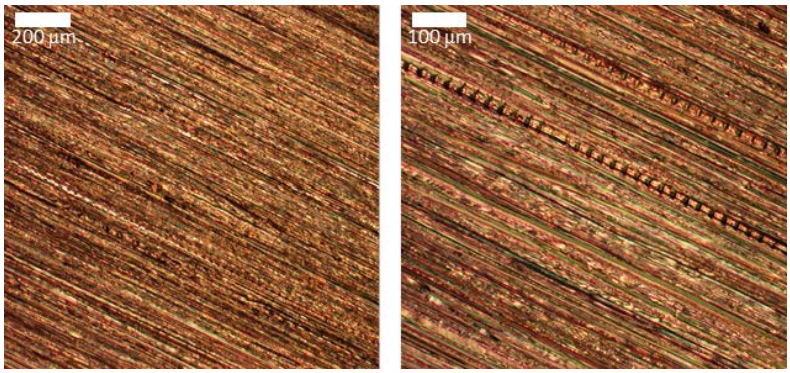

Figure 3-2. *Optical microscopy images of abrasively cleaned samples.*

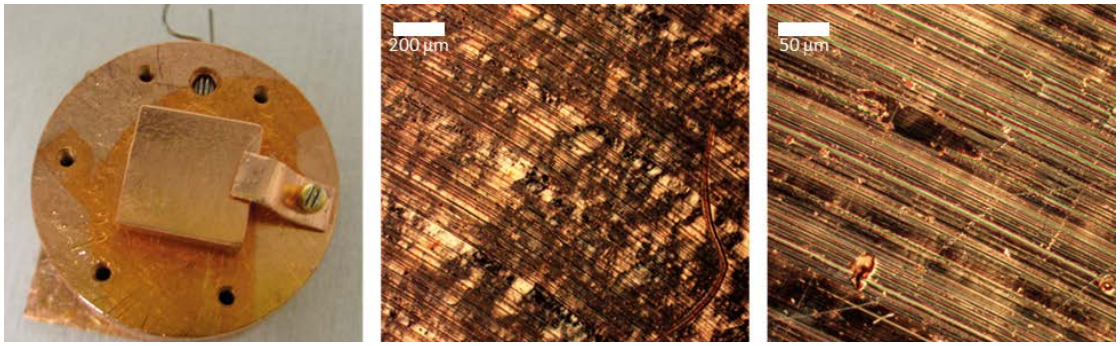

Figure 3-3. *CO_2 cleaned sample attached to an XPS sample holder (left). Optical microscope images of a CO_2 cleaned surface (centre and right).*

Various parameters were tested for laser cleaning. The contact angle was 0° for all samples (complete wetting of the surface). For the samples prepared for XPS, the following parameters were used: pulse frequency 200 kHz, scanning width 220 %, focal length 120 mm and power 100 W.

The sample was swept manually with the laser beam eight times diagonally. The curved grooves of the as-received samples disappeared during the cleaning. The sample surface varied in colour, with some darker areas as shown in Figure 3-4. Optical microscopy images revealed lines of pearl-like protrusions parallel to the laser beam (perpendicular to the sweeping direction).

3.1.7 Plasma cleaning

The PlasmaBeam PC cleaning equipment was provided by Diener Electronic. The plasma cleaning is based on the bombardment of ionized plasma at the sample surface, chemical reactions between the plasma and the surface and UV light emitted by the plasma. The PlasmaBeam PC was operated with air and Formier 5 (95 % N_2, 5 % H_2). The sample attached to the jig was shifted beneath the plasma beam using a Lego Mindstorm robot. In addition to the plasma gas, the distance between the plasma nozzle and the sample surface and the speed of the robot were adjusted to optimise the cleaning time.

Generally, the contact angles on plasma-cleaned samples were relatively low, 15–40°. The shorter distance between the nozzle and the sample as well as the EtOH rinsing before the plasma cleaning reduced the contact angle. Significant differences in the contact angles were not observed between plasma cleaning with Formier 5 and air. The temperature of the sample and the jig increased significantly during the cleaning procedure. The temperature of the plasma beam was 300–500 °C.

For XPS measurements, the distance between the nozzle and the sample was fixed at 3 mm, and the speed of the robot was fixed at 40 arb. unit.

Figure 3-5 shows the optical microscopy images of the plasma-cleaned surface. No clear changes in the surface morphology were observed.

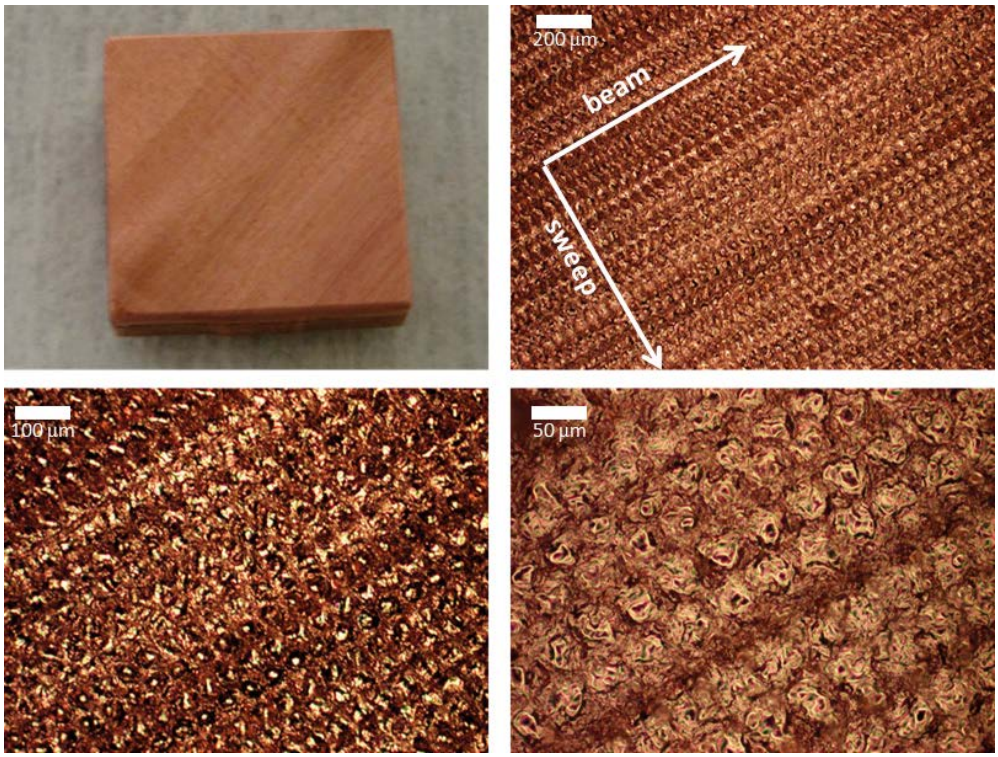

Figure 3-4. *Laser cleaned sample (top left) and optical microscopy images of the surface..*

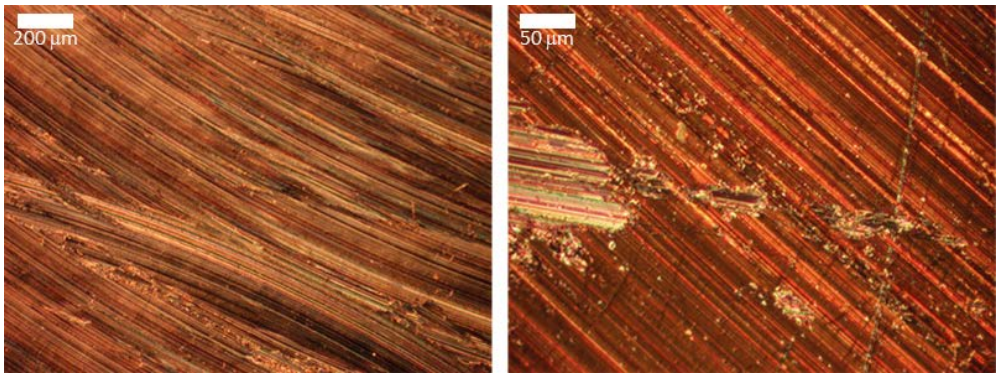

Figure 3-5. *Optical microscopy images of plasma-cleaned surfaces.*

3.1.8 Stainless steel brush cleaning

Mechanical cleaning with a stainless steel brush was performed using a stainless steel crimped wire wheel brush (Osborn International GmbH, article no: 70902 504 341, FN 1083-2, wire diameter 0.20 mm). The stainless steel brush cleaning removes material from the surface and leads to a grooved surface morphology with a rougher surface compared with abrasive cleaning with the Scotch Brite grinding wheel (Figure 3-6). The contact angle for the samples varied between 60° (perpendicular) and 81° (parallel to the grooves).

3.1.9 X-ray photoelectron spectroscopy measurements

Four samples for each cleaning method were investigated with X-ray Photoelectron Spectroscopy (XPS). All four samples were cleaned using the same cleaning procedure and parameters (described in sections 3.1.4–3.1.8). The freshly cleaned samples were introduced into the UHV system within 15 min after the cleaning procedure, and the load lock was evacuated from atmospheric pressure before transferring the sample to the analysis chamber with a base pressure below 1×10^{-10} mbar. The aged samples were measured after two weeks of storage under atmospheric conditions. The long-term storage time was about 8 months.

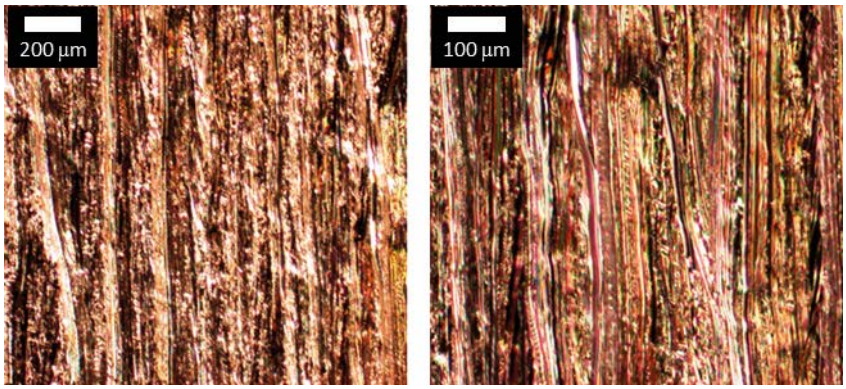

Figure 3-6. *Optical microscopy images of stainless steel brush-cleaned surfaces.*

In XPS, non-monochromatised Mg K_α X-rays (1253.6 eV) were utilized for excitation, and the measurements were performed at a normal (0°) emission with a detection area of ~600 µm in diameter. Source-to-analyser angle was 54.7° (magic angle), and the angle for the incoming x-rays with respect to the sample surface was 35.3°. The XPS experiments began by measuring a survey spectrum, which allows the identification of the elements at the surface within the sampling depth. All samples were examined at two different locations on the sample surface. If the survey spectra were clearly non-identical, then high-resolution spectra of all the elements were recorded at both locations.

The surface elemental concentrations and chemical states of the compounds were identified by analysing the high-resolution spectra of the transitions observed in the survey scan. After subtracting a Shirley- or linear-type background, the spectral components were fitted with a combination of Gaussian and Lorentzian line shapes using CasaXPS software.

Depth profiling by repeated cycles of XPS measurements and Ar^+ ion sputtering was performed on the as-received sample and on one sample from each cleaning method. Ar^+ ion sputtering removes atomic layers from the sample surface. A sputtering rate of 0.064 nm/s was determined using an Al_2O_3/Si reference for the depth profiles (DPs) performed in 2014. The sputtering rate for the stainless steel brush depth profile (Pos #5N) was determined as 0.031 nm/s. The angle of the sputter gun with respect to the sample surface was 90°. The sputtering yield of different materials is not constant, and the sputtering rate of copper samples most likely differs from that determined for the Al_2O_3/Si reference. The chemical states of the elements may change upon sputtering; however, useful information on the elemental depth distribution can still be obtained. The surface roughness of the sample affects the local sputtering rate, thus affecting the analysis of the elemental in-depth distribution. When depth profiling macroscopically rough surfaces, as was the case in the samples studied in this research, the surface contains shadowed areas that are not sputtered at a normal rate. Because the surface roughness was unknown for the as-received samples and changed during the different cleaning procedures, the depth resolution was not corrected in the analysis of the depth profiling results.

Most of the XPS signal (95 %) is acquired from the surface layer with the thickness defined by the sampling depth. The sampling depth depends on the kinetic energy of the outgoing electrons which depends on the incident photon energy used and the binding energy of the element. For the samples studied in this research, the sampling depth varied between 2 and 10 nm.

3.2 Results

A detailed description of all measurements is given in Appendix 1, and the primary results are provided below.

3.2.1 Elemental composition

Figure 3-7 shows the survey spectra of all the samples: as-received sample (no cleaning), sputter-cleaned Cu sample (impurities and oxide layer removed by Ar^+ ion sputtering) and sputter-cleaned Cu sample followed by air oxidation for 15 min (reference for the level of atmospheric impurities), as well as samples followed by the cleaning procedure. The relative elemental surface concentrations can be found in Appendix 1. In addition to copper, carbon and oxygen are observed on all the samples. C and O impurities originate from exposure to atmospheric conditions and surface impurities. Other impurity elements at the surface originate either from the Cu sample itself or from the cleaning method.

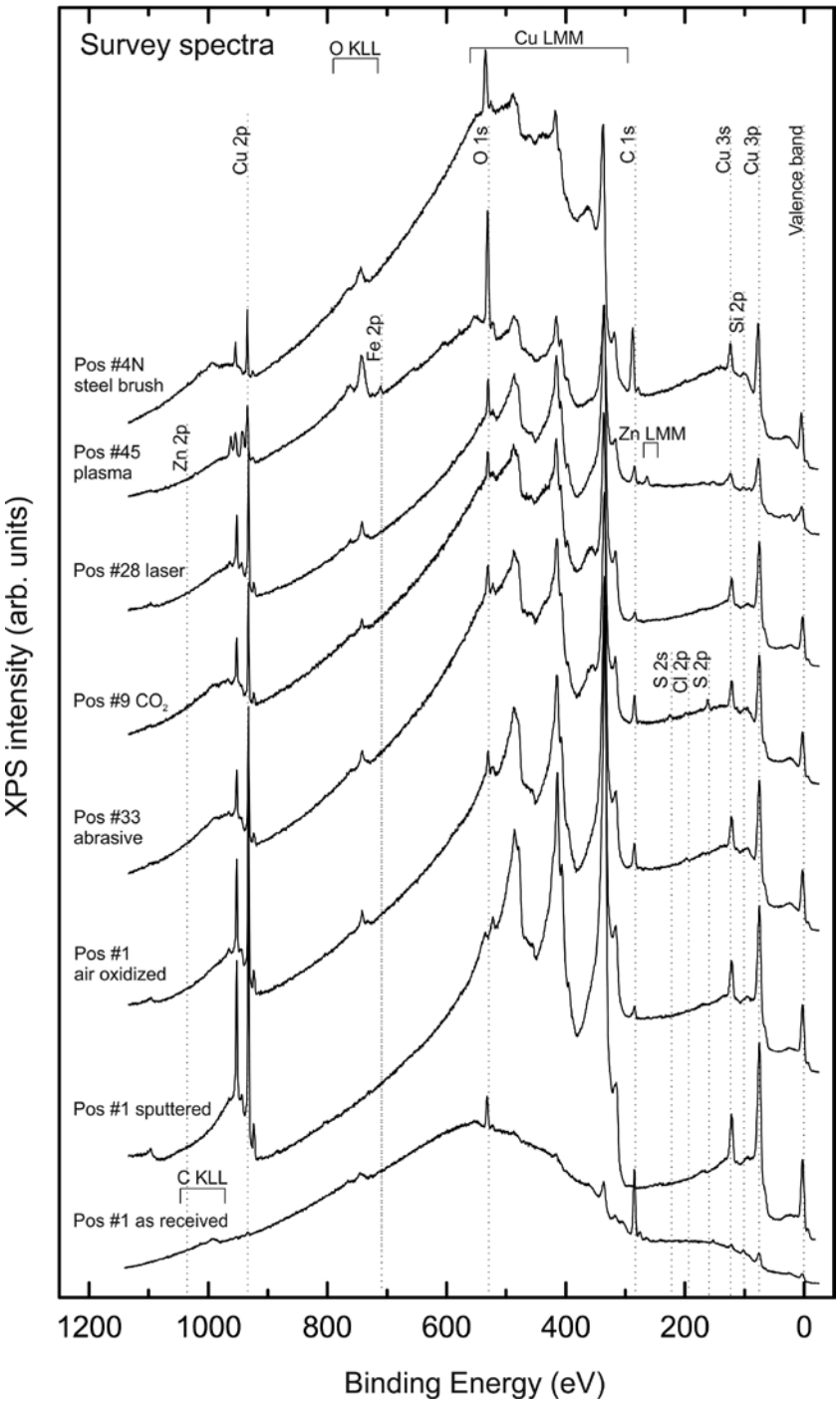

Figure 3-7. *XPS survey spectra of the reference samples and samples cleaned using different cleaning procedures.*

The relative surface concentration of C is the highest on the stainless steel brush-cleaned sample (65 at-%) followed by the abrasively cleaned samples (41 at-%), CO_2 (35 at-%), plasma (20 at-%) and laser (15 at-%). The relative surface concentration of O is highest on the plasma-cleaned samples (49 at-%), followed by laser (31 at-%), stainless steel brush (23 at-%) and CO_2 and abrasive (both 22 at-%) cleaning. The highest amount of other impurities (elements other than C, O and Cu) was observed on the plasma-cleaned (15 at-%) and CO_2-cleaned (8 at-%) samples, whereas abrasive (2 at-%) and stainless steel brush (1 at-%) and laser cleaning (0 at-%) removed virtually all elements other than C, O and Cu. The relative surface concentrations were calculated as averages of freshly prepared samples (excluding aged samples and additional plasma-cleaned samples Pos #43 and #44). See Appendix 1 for detailed data.

Si and Cl were observed on the as-received samples. CO_2 cleaning introduced sulphur (5 at-%) to the surface. Plasma cleaning resulted in an overlayer containing Fe (3 at-%), S (1 at-%), Zn (<1 at-%) and N (6 at-%) at the surface. No new elements at the surface were observed after abrasive and laser cleaning. Only laser cleaning removed all Cl.

3.2.2 Chemical state

The chemical composition of C, O and Cu was analysed for each sample. In addition to different elemental compositions, the cleaning methods also result in different chemical compositions of the aforementioned elements. Figure 3-9 and Figure 3-10 show the high-resolution spectra of C 1s, O 1s and Cu 2p of one sample from each cleaning method. Two chemical states are observed for most of the samples in the O 1s spectra, O-Cu and O-C/=C. The latter also includes the signal from other surface compounds containing oxygen species, such as SiO_2, OH, etc.

The copper signal is attenuated on samples with a high amount of impurities. The chemical states of copper were determined from the Cu LMM Auger transitions (X-ray-excited Auger electron transitions) by fitting the region with Cu^0, Cu^+ and Cu^{2+} reference spectra (Hirsimäki et al. 2005). This method allows the determination of the relative amount of metallic copper, Cu_2O and CuO. An example of the data analysis is shown in Figure 3-8, illustrating that the changes in the chemical states of copper can be readily resolved.

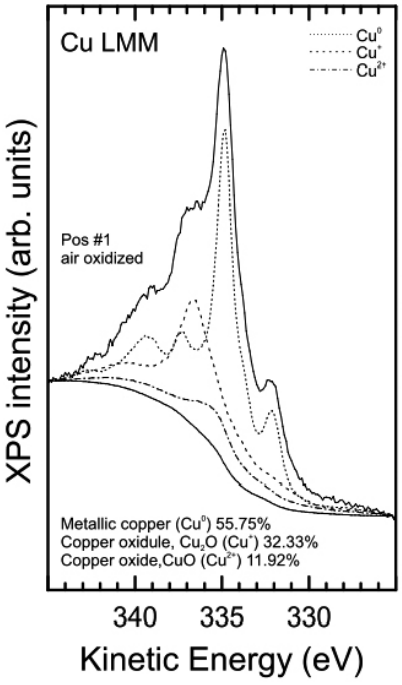

Figure 3-8. *X-ray-excited Auger Cu LMM transitions of the air-oxidized sample together with reference spectra (Hirsimäki et al. 2005).*

No significant elemental or chemical differences were observed with samples manufactured with and without cutting fluids, except for the stainless steel brush-cleaned samples in which the amount of C impurities was higher on samples with cutting fluid. The largest changes in the chemical states are most likely due to the different temperatures used during cleaning. Ageing typically leads to an increased relative surface concentration of C and O and further oxidation of Cu.

3.2.3 Depth profile

The surface impurity overlayer and copper oxide thickness cannot be accurately determined due to the rough surface morphology of the investigated samples. However, the relative thicknesses can be compared by monitoring the increase in the relative surface concentration of metallic Cu during the depth profiling of each cleaning method. The apparent thickness (sputtering time) of an overlayer may increase with increasing surface roughness. The Cu^0 concentration was determined from the X-ray-excited Auger Cu LMM transition.

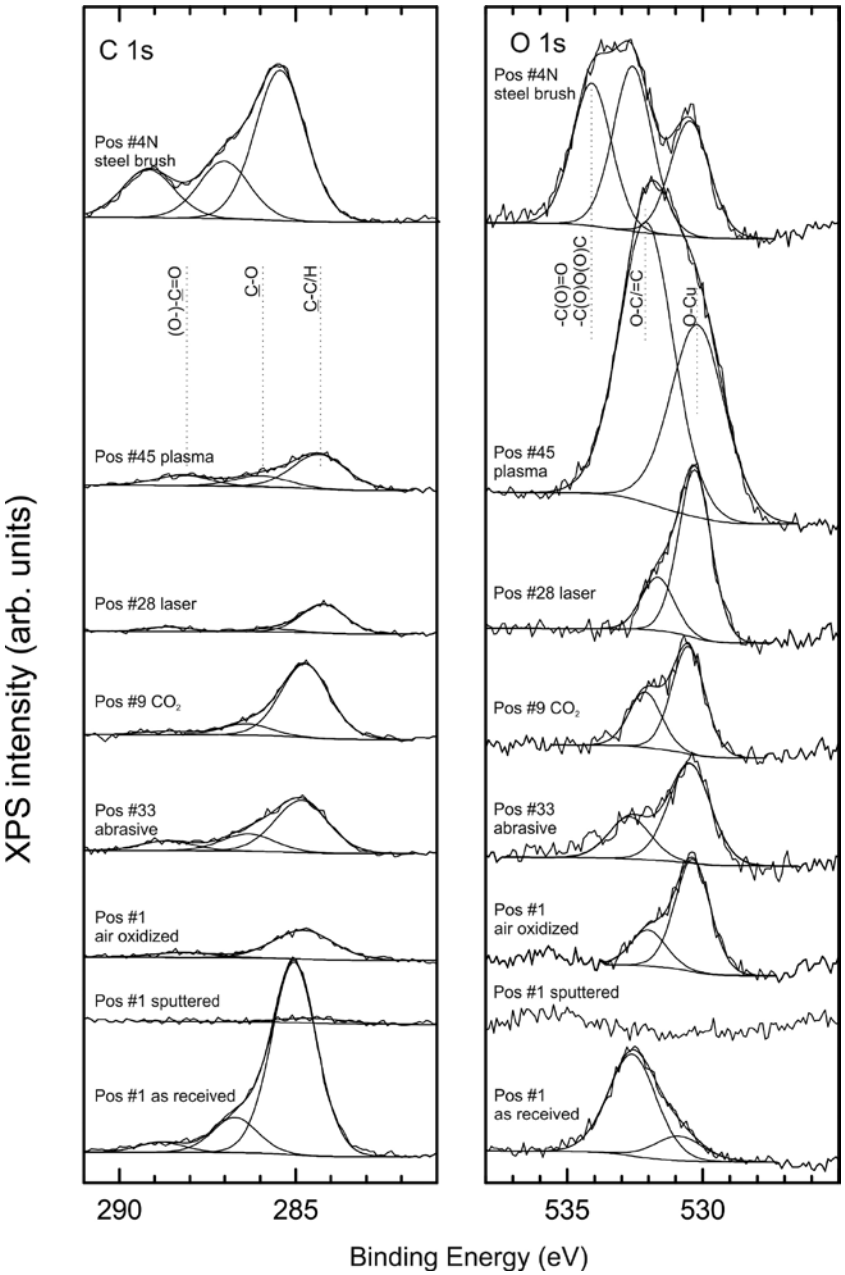

Figure 3-9. *High resolution C 1s and O 1s XP spectra of the reference samples and samples cleaned using different cleaning procedures. The figure shows the fitted peaks profiles for different chemical states together with the data.*

The depth profile of the stainless steel brush-cleaned sample was determined using different sputtering geometries and speeds. In Figure 3-11, the sputtering speed of the steel brush-cleaned sample is converted to correlate with earlier depth profiles. The sputtering times were determined for atomically flat and uniform samples. Differences in the macroscopic roughness can lead to differences in the sputtering speed, and organic impurities may have a different sputtering speed than the copper oxides. Thus, the depth profile of the steel brush-cleaned sample is not fully comparable to the other depth profiles.

Figure 3-11 shows that abrasively cleaned, the stainless steel brush cleaned and CO_2-cleaned samples have the thinnest overlayers (impurities and an oxide layer). The laser cleaning may slightly reduce the overlayer thickness, and plasma cleaning results in a thicker overlayer than that observed on the as-received sample.

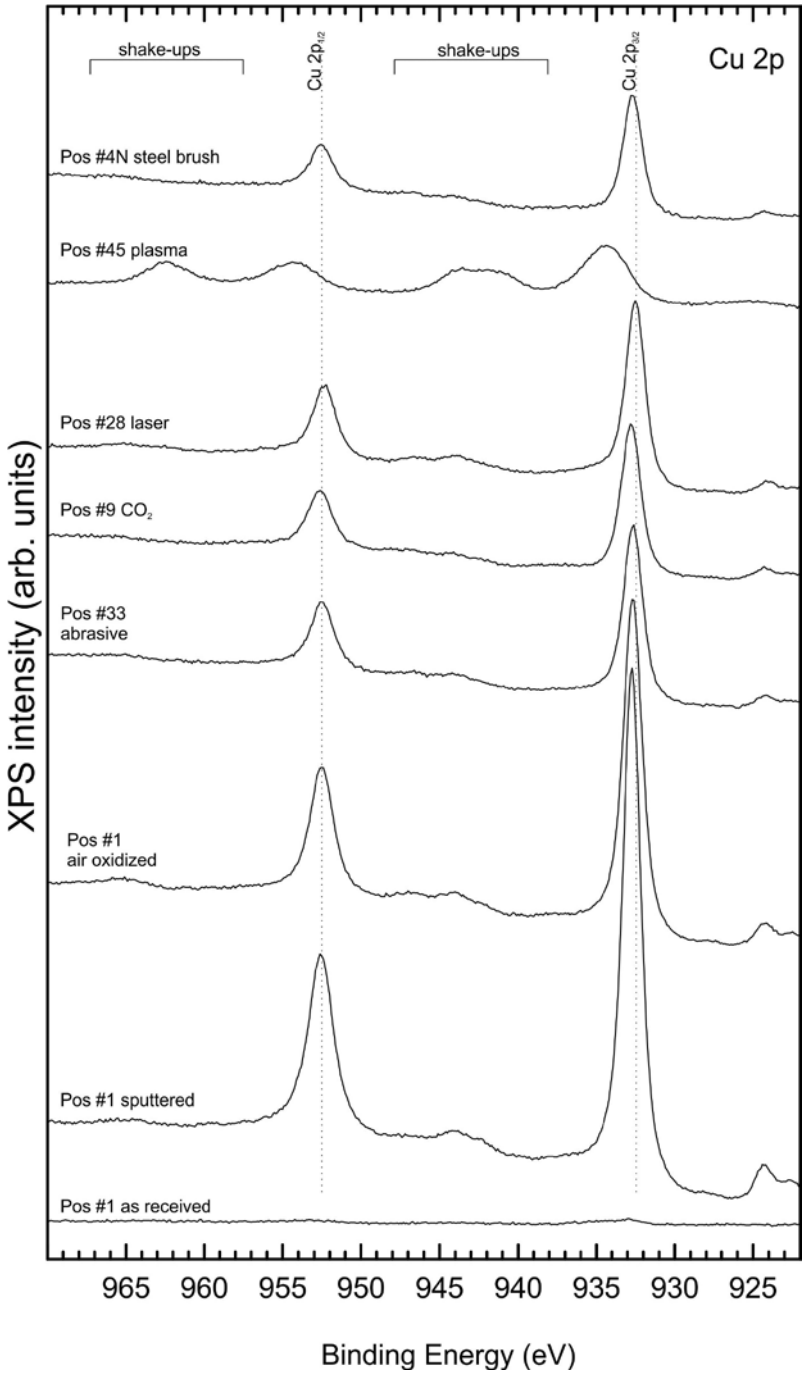

Figure 3-10. *High resolution Cu 2p XP spectra of the reference samples and samples cleaned using different cleaning procedures.*

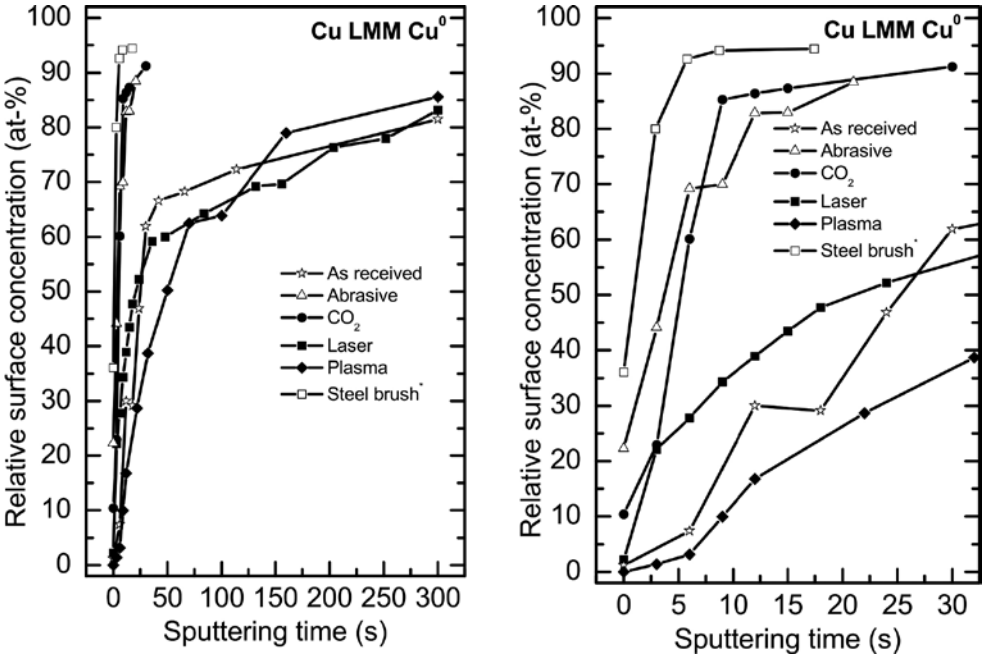

Figure 3-11. *Relative surface concentration of metallic Cu determined from the X-ray-excited Auger Cu LMM transition as a function of sputtering time. The figure on the right illustrates the initial stages of depth profiling. Note that the DP of the stainless steel brush-cleaned sample was performed with different sputtering speeds (see text for details).*

3.3 Discussion and Conclusions

The cleaning methods not only remove impurities from the surface but also affect the thickness of the oxide layer. The thinnest oxide layers were observed after abrasive, CO_2 and stainless steel brush cleaning. The use of cutting fluids does not affect the surface cleanliness or the oxide layer thickness. A summary of all of the results can be found in Table 3-1. Ageing increases the amount of C and O impurities on the sample surfaces and the oxide layer thickness.

The steel brush and the abrasive cleaning methods are the simplest, utilizing standard power tools. The plasma, laser and CO_2 cleaning protocols require more specialized equipment. Therefore, cleaning with an abrasive wheel appears to be a simple method that results in a thin oxide overlayer and a small amount of impurities.

The results should be viewed as an initial investigation of the capability of the cleaning methods investigated. Most of the cleaning protocols can be optimised. If the distance between the workpiece and the laser head is controlled, then less variance in the chemical composition of the surface is expected (see Appendix 1 for more details). The contamination during CO_2 cleaning might be removed if a cleaner, dedicated system is used.

Table 3-1. Summary of the characteristics of each cleaning method. The oxide thickness is determined from the depth profiles of the Cu^0 LMM signal. The surface contamination is the sum of the elements, except for Cu, O and C. See Appendix 1 for more details.

Method	Oxide thickness	Surface fraction of met. Cu [%]	Surface contamination [%]	Affected by cutting fluids	Complexity
Abrasive cleaning	Low	10–18	1–2	No	Low
CO_2 cleaning	Low	4–7	5–9	No	Medium
Laser cleaning	Medium	9-12 (1 for dark areas)	0	No	High
Plasma cleaning	High	0	4–15	No	Medium
Stainless steel brush	Low	1–8	0–1	Yes	Low
As received	Medium–High	0	5	–	–
Clean – air oxidised	Very Low	31	0	–	–

4 Optical properties of oxide films

Copper oxide has optical properties that are different from copper metal. Therefore, it is instructive to elucidate the effect of the optical response, the colour of the surface, on the oxide thickness. The specular reflected intensity of the light, considering the interference in the thin film, can be calculated using the transfer matrix method (Born and Wolf 1992) or, as in this study, using Paratt's recursion algorithm (Parratt 1954). As applied in this study, these methods do not consider any surface roughness. Also, in order to simplify the calculation the copper oxide layer is assumed to only consist of Cu_2O. The refractive indices are taken from Lynch and Hunter (1997) and Ribbing and Roos (1997). The optical constants for copper were also discussed by Babar and Weaver (2015).

Figure 4-1 shows the calculated normal-incidence reflectivity calculated for a copper surface, as well as for a copper surface with an additional oxide layer of 10 nm. The step at approximately 550–600 nm occurs because the energy of the incident light is sufficient to excite the 3d electrons. This results in the more red colour for copper compared to, for example, silver, where the same edge resides in the ultraviolet part of the spectra and the reflectivity spectra is flatter in the visual region. Ehrenreich and Philipp (1962) discussed how the electronic structure relates to the optical properties. When copper is oxidised, the electronic structure changes; consequently, the reflected spectra also changes. A 10 nm thick oxide film causes a change in the reflectivity, especially below the step at 550–600 nm, as shown in Figure 4-1.

The calculated spectral response can be transformed into perceived colours through CIE 1931 XYZ colour spaces (CIE n.d). These XYZ colours can be transformed to sRGB colours that are suitable to view in ordinary computer programs. This linear transformation is specified in IEC 61966-2-1:1999. The object is assumed to be illuminated by the CIE standard illuminant D65, which corresponds to daylight. The code to calculate the spectral response is given in Appendix 2 and the result can be seen in Figure 4-2. For a copper surface without an additional oxide layer, the surface appears slightly pink and becomes more brown/orange when the oxide thickness increases to 15 nm. At 20–25 nm, the colour changes to purple.

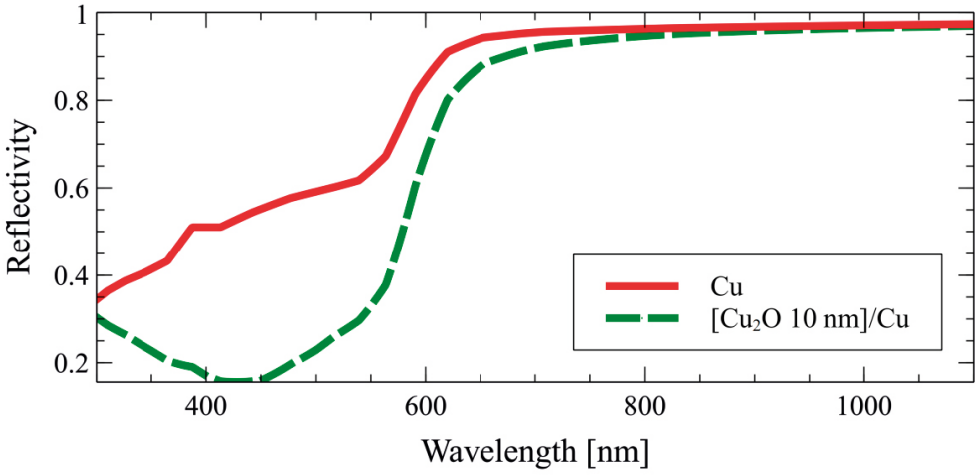

Figure 4-1. *The calculated normal-incidence specular reflectivity as a function of wavelength for a copper surface (red full line) and a 10 nm Cu_2O film on copper (dashed green line).*

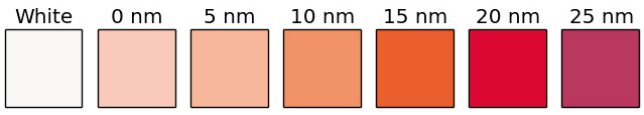

Figure 4-2. *Calculated normal incidence specular colours of a Cu_2O film as a function of film thickness (indicated above each square). As a comparison, the leftmost square should appear white (a flat spectral response). Note that different viewing media yield slightly different colour appearances.*

5 Welding experiments

During welding surfaces can be oxidised if exposed to oxygen in combination with elevated temperature. Since FSW is a solid state welding process no oxides will form in the weld material after and during the joint line has been stirred. Any oxides found in the weld material have formed either at the joint line or at the outer surface before joining and subsequently stirred into the material. Therefore it is expected that the weld material below the down travel sequence could have a larger amount of oxide particles since this area has been heated before joined (Björck 2015).

5.1 Experimental details

To investigate the resulting weld quality with the new gas shield, three different trial welds were welded. The different welds are summarised in Table 5-1. All joint surfaces were prepared according to a predefined scheme. The joint surfaces were grinded using a 3M Scotch-Brite PF-ZS (Part Nr. 07212A. Very Fine) abrasive wheel. Steps and corners were brushed with a stainless steel brush. Then, the surfaces were cleaned with ethanol using TORK Specialist Cloth. The cleaning was determined as acceptable by the appearance and colour of the surface – a homogenous distribution of grind marks as well as a bright "pink" colour. The wipe cleaning test was judged by wiping an ethanol-moistened TORK Specialist Cloth with a firm pressure around the full circumference of the lid/ring. If the cloth remained stain-free compared to a moist fresh cloth, then the joint surface was deemed clean. An example of the resulting weld surfaces can be seen in Figure 5-1. After cleaning, the lid was placed on the welding ring within a few hours. Then, the assembly was left overnight, more than 15 h, in a laboratory environment before mounting it in the welding machine.

Table 5-1. Summary of the different welds prepared.

	FSWL108	FSWL109	FSWL110
External shielding gas	Ar	Ar	Ar + 2 at-% H_2
Internal shielding gas	None	N_2	N_2 + 2 at-% H_2

The first weld, FSWL108, was prepared with Ar (99.99 % purity) shielding gas. The oxygen content in the gas shield was monitored during welding with the above-mentioned oxygen monitors. The multiplexer logger was misconfigured during the experiment, and the oxygen content was not recorded digitally; thus, the values were noted manually.

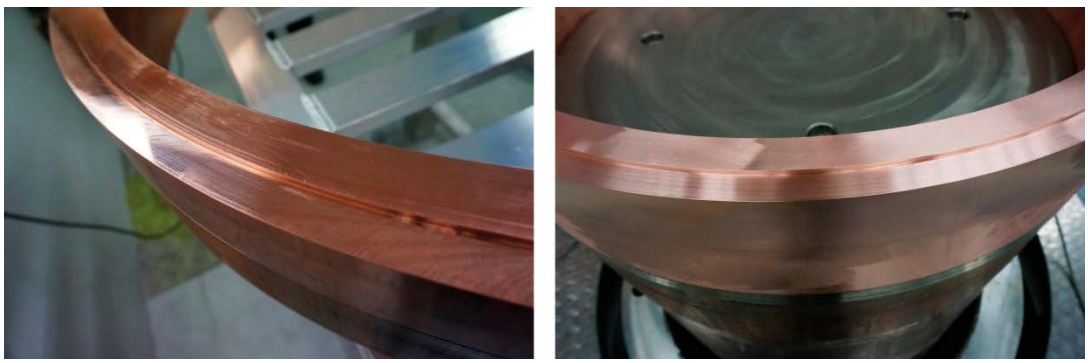

Figure 5-1. *The ring of weld FSWL109 as machined (left) and after joint preparation (right). Note the colour change of the joint surfaces from a dark copper colour (oxidised) to a "pink" colour.*

The second weld, FSWL109, was prepared with an additional nitrogen shielding gas on the inside. To achieve a protective gas shield on the inside of the canister, an O-ring-sealed steel plate was placed beneath the welding ring. The steel plate contained KF flanges for gas sampling, a vacuum pump (8 l/s oil sealed rotary vane pump supplied by Löwner Vacuumservice AB, model 2SZ-8B), Pirani vacuum gauge (MKS series 345 gauge with MKS 945 controller, pressure range 10^{-4}–130 mbar), piezoelectric pressure gauge (S04-HT from Sensor-technik Wiederman GMBH, pressure range 0–2 bar) and a gas line connection (Figure 5-2). The inside of the welding ring was pumped down to a pressure of 2–3 mbar and was flushed with nitrogen (99.95 % purity) three times. The major leak in the system was previously identified to be the joint line. Before pumping down the inside the first time, care was taken to ensure that the oxygen content in the external gas shield was below 100 at-ppm. Nitrogen was used for flushing because it is lighter than oxygen. The ring was filled from the bottom, and nitrogen floated above any oxygen. After the last flushing with nitrogen the gas flow rate was adjusted so that an overpressure was maintained during the entire welding sequence inside the ring. The oxygen content inside the ring was monitored with a Rapidox 1100 ZR3.

The third weld, FSWL110, was prepared using the same procedure as FSWL109, except that the shielding gases contained 2 at-% H_2. Hydrogen will reduce copper oxide to pure copper and water. The oxygen content in the gas shield during welding could not be monitored with Rapidox 1100 ZR3 and Rapidox 1100 ZF because the high temperatures of the zirconia sensors cause all of the oxygen to form water if hydrogen is present. Instead, an electrochemical oxygen analyser, Rapidox 1100LF, was used. One section, which was approximately 60° in size, away from the start section of the joint surfaces was cleaned with a steel brush instead of the normal procedure with the 3M Scotch-Brite PF-ZS for comparison. The use of a steel brush was part of the recommended practice from the first development stages at TWI (Andrews 2004, pp 43–44).

After the welding sequence was completed, the welded components were allowed to cool in the protective atmosphere for at least 30 min in order to avoid discoloration. Then, the welds were photographed and machined to their final dimensions (Cederqvist 2014). The objects were investigated with ultrasonic inspection and X-ray radiography (data not shown).

Samples for destructive testing were cut according to a pre-defined scheme around the start (Figure 5-3) and at a steady state (Figure 5-4). The area that was expected to contain the largest amount of oxides was where the tool reached the joint line at the start (Björck 2015). The samples extracted at 180° are considered representative of the remainder of the weld.

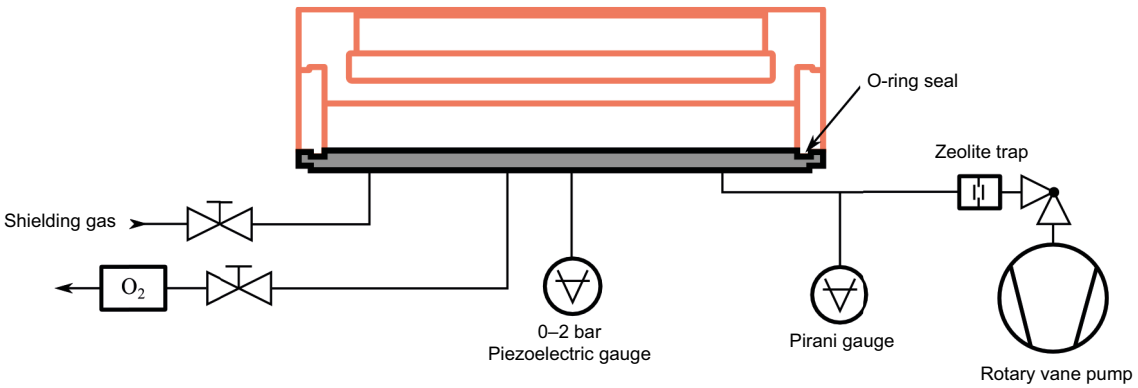

Figure 5-2. *A schematic picture of the setup for the experiments with an internal shielding gas. The orange lines represent the ring and lid. The steel plate beneath is coloured grey.*

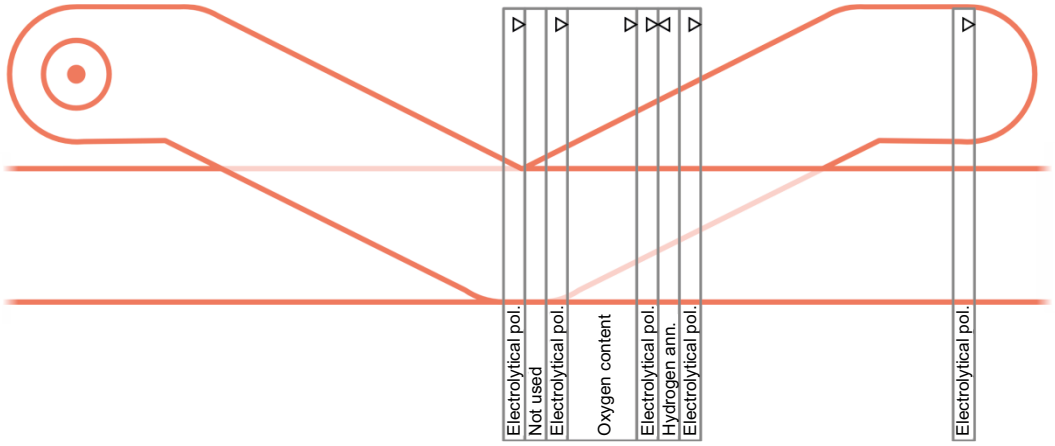

Figure 5-3. *Samples extracted for tests around the start-stop part of the weld. The red lines are the trace of the shoulder. The exit hole is seen in the left upper part. The start is on the upper right (defined as 0°). The leftmost sample was only removed for FSWL108 and FSWL109.*

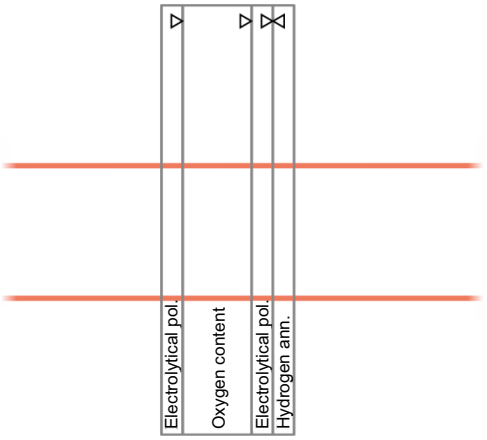

Figure 5-4. *Samples extracted from the steady state part of the weld. The samples are located approximately 180° from the start of the weld. The red lines show the trace left by the shoulder.*

The oxygen content measurements were conducted using LECO equipment at 15 different measuring points per weld cross section sample and two measuring points in the base material. The weld area of the extracted samples was identified with a macroetch using HNO_3 (Figure 5-5), and a picture was taken. Samples from different regions of the pictures were marked and then overlaid onto the actual sample pieces for cutting (see the two rightmost figures in Figure 5-5, sample size approximately $5 \times 5 \times 20$ mm^3). Hydrogen annealing studies were also performed according to ASTM B577-16, method B. The weld samples were annealed in a hydrogen atmosphere containing at least 10 % H_2 at a temperature of 850 ± 25 °C for 20 to 40 min. The samples were subsequently polished and observed under a microscope. The presence of copper oxide can be seen as cavities that arise from the water pressure as the copper oxide is reduced. The amount (on a 1–5 scale) and placement (cross grain (A), within grain (B) and grain boundary (C)) of the oxides were characterised using the ASTM F68-10 comparison chart. Measurements were conducted by LUVATA Oy in Pori, Finland. The hydrogen annealing measurements complements the oxygen content measurement since the former measure the local distribution of copper oxide particles whereas the oxygen content measures the global average over the sampling volume.

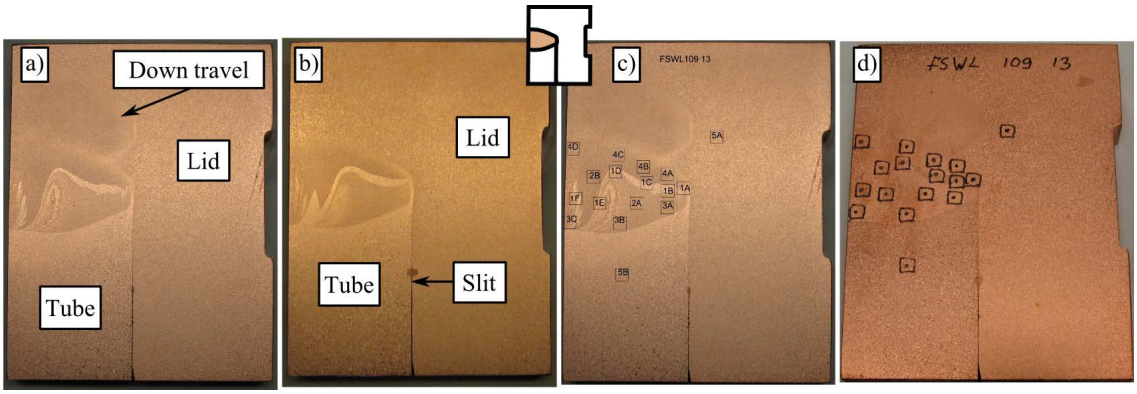

Figure 5-5. *Pictures from the macroetch of samples FSWL109 13° (a) and FSWL109 175° (b) identifying the different parts of the welded material. Sample FSWL109 13° contains part of the down travel sequence that can be seen as a second weld zone above the one at the joint line. c) shows the preliminary marking for sample extraction and d) the final identification before cutting. The small inset in the middle shows the orientation of the samples.*

Many samples, some of which appear in Figure 5-3 and Figure 5-4 marked with electrolytic polishing, were investigated by EXOVA AB in Linköping Sweden (Lantz 2015, Reuterswärd and Lantz 2015a, b) under accreditation according to SS-EN 1321:1997. The samples were polished using Emery paper and diamond slurry. The samples were electrolytically polished using a mixture of 250 ml H_3PO_4, 50 ml propanol, 250 ml ethanol, 500 ml distilled water and 5 g urea. The samples were polished with a voltage of 9 V for approximately 60 s using a LectroPol-5 from Struers ApS. The samples were subsequently studied using an optical microscope.

5.2 Results and Discussion

5.2.1 Welding

During welding FSWL108 with only an external gas shield, it was noticed that smoke appeared from the non-cleaned areas below the welding area within the gas shield, especially during the beginning of the weld. This was interpreted as combustion of cutting fluid residues remaining after machining since this was accompanied with a dip in the oxygen content. The oxygen content was < 50 at-ppm in the gas shield during the entire welding, as shown in Figure 5-6. The resulting weld can be seen in Figure 5-8.

For FSWL109, the entire ring was cleaned to avoid any smoke during welding. The oxygen content was < 50 at-ppm during the entire weld (Figure 5-6). An overpressure of at least 0.05 bar was maintained in the internal gas shield by regulating the inflow. During welding, patches of a darker colour (Figure 5-9) formed on the lower side of the shoulder trace at some locations. Using the colour comparison chart in Figure 4-2, it can be determined that the oxide thickness is definitely below 20 nm and is most likely below 10–15 nm. The maximum temperature measured in the weld is 915 °C (Björck 2015). Figure 5-7 shows the oxide thickness evolution of a few different scenarios, with different maximum temperatures and different oxygen concentrations, calculated using Björck and Elger's (2013) oxidation model. A maximum temperature of 900 °C at 50 at-ppm oxygen yields an oxide thickness of 10 nm, which is in agreement with the surface colour. The patches are localised on the tube side where the temperature is higher (Björck 2013). FSWL108, however, did not show the same oxide patches that were observed on FSWL109. This is interpreted to be due to the smoke that evolved during welding. Combustion of cutting fluids consumes oxygen and can form reducing species, such as hydrogen gas. Additionally, a reduction from, for example, 10 nm to 5 nm in oxide thickness on the copper surfaces causes the colour change to nearly disappear. The oxide thickness of the as-welded surface has an indirect correlation to the oxide content in the weld since oxides can be formed due to a high oxygen content in the gas shield after joining or the oxygen content on the inside can be higher or lower than on the outside. However, a thick oxide layer on the outside indicates the possibility of a high amount of oxides in the weld material.

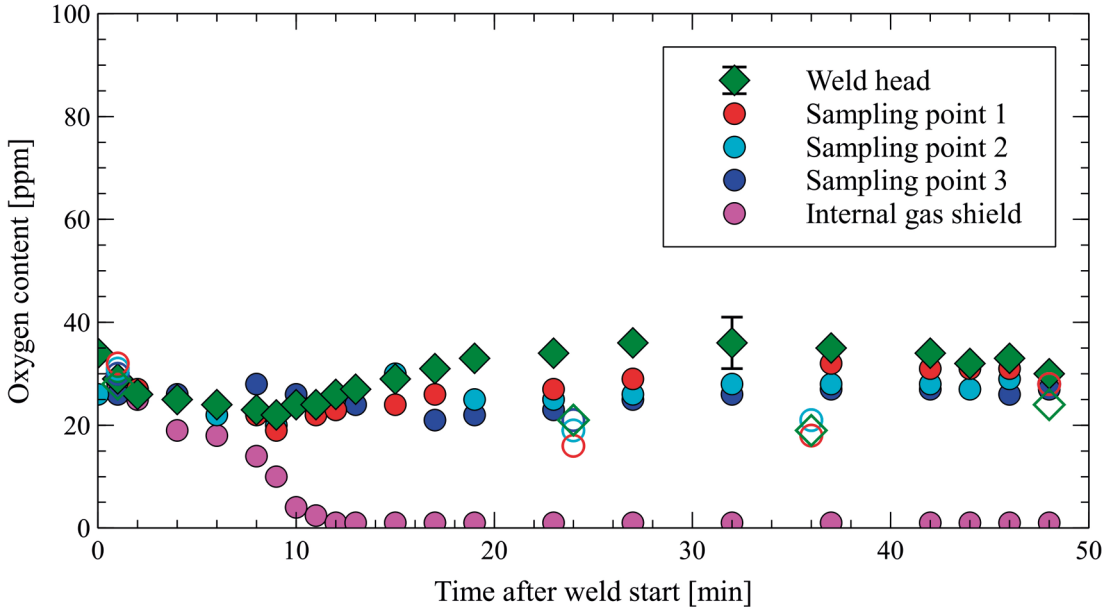

Figure 5-6. *Oxygen content during welding of FSWL109, filled symbols, and FSWL108, open symbols. The measurement locations are indicated by the colour and shape, as shown in the legend. The absolute accuracy (95 % confidence interval) is shown for a single data point only but valid for all measurements.*

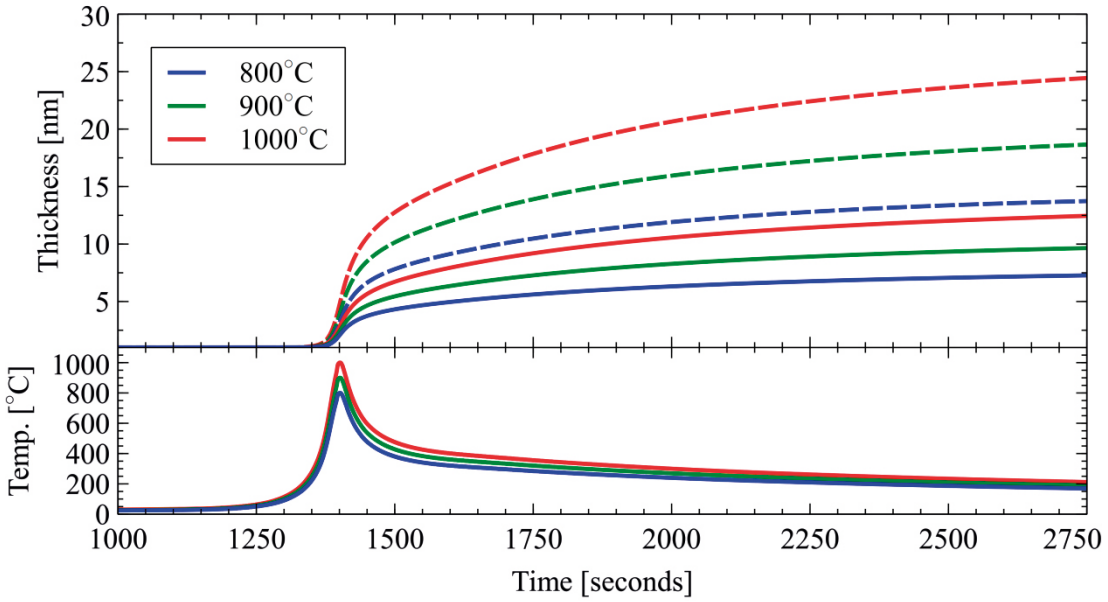

Figure 5-7. *The calculated oxide thickness (top) for different temperature profiles (bottom). Dashed lines correspond to 100 at-ppm oxygen, and full lines correspond to 50 at-ppm oxygen. The colour defines the maximum temperature, as given by the legend. The temperature profile is a rescaled measured profile from Björck (2013), angle 181.5 degrees.*

FSWL110 was welded in a hydrogen-containing atmosphere in which a zirconia oxygen sensor does not function; therefore, an electrochemical sensor was used. However, the reading did not stabilise over the entire welding period because of the sensor's long response time. The oxygen content at the welding head was measured as 148 at-ppm at the start of the weld and decreased to 117 at-ppm at the end of the weld. An overpressure of at least 0.05 bar was maintained in the internal gas shield throughout the welding sequence. The resulting weld surface can be seen in Figure 5-10. This weld was shinier than the two previous welds, and no discolouring on the weld was observed.

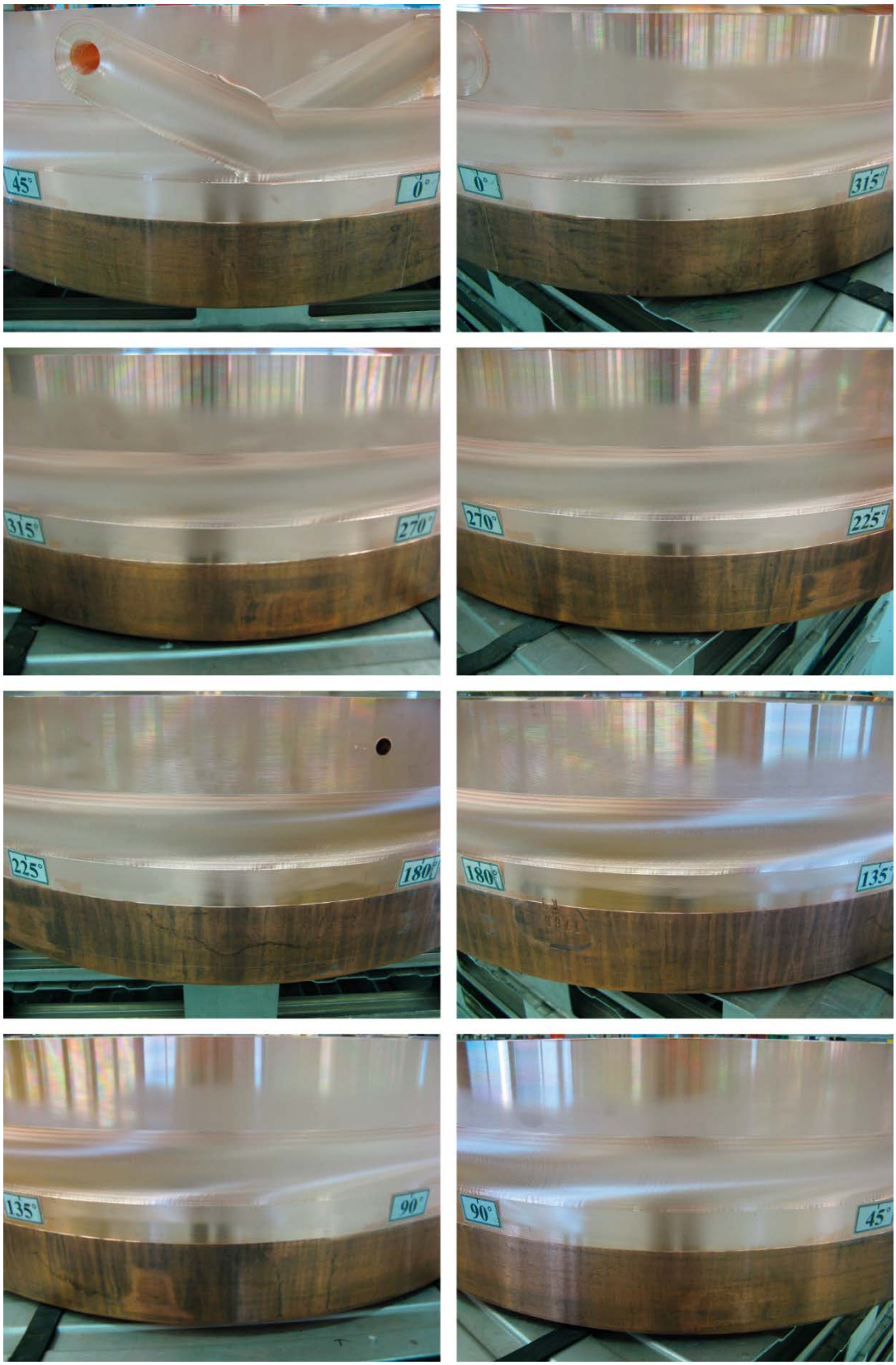

Figure 5-8. *Photographs of the weld with only external gas shielding (FSWL108). The darker, lower surface was not cleaned or machined to a final diameter. No discolouring could be identified after welding which is interpreted as an oxide thickness below 5 nm, see text for details.*

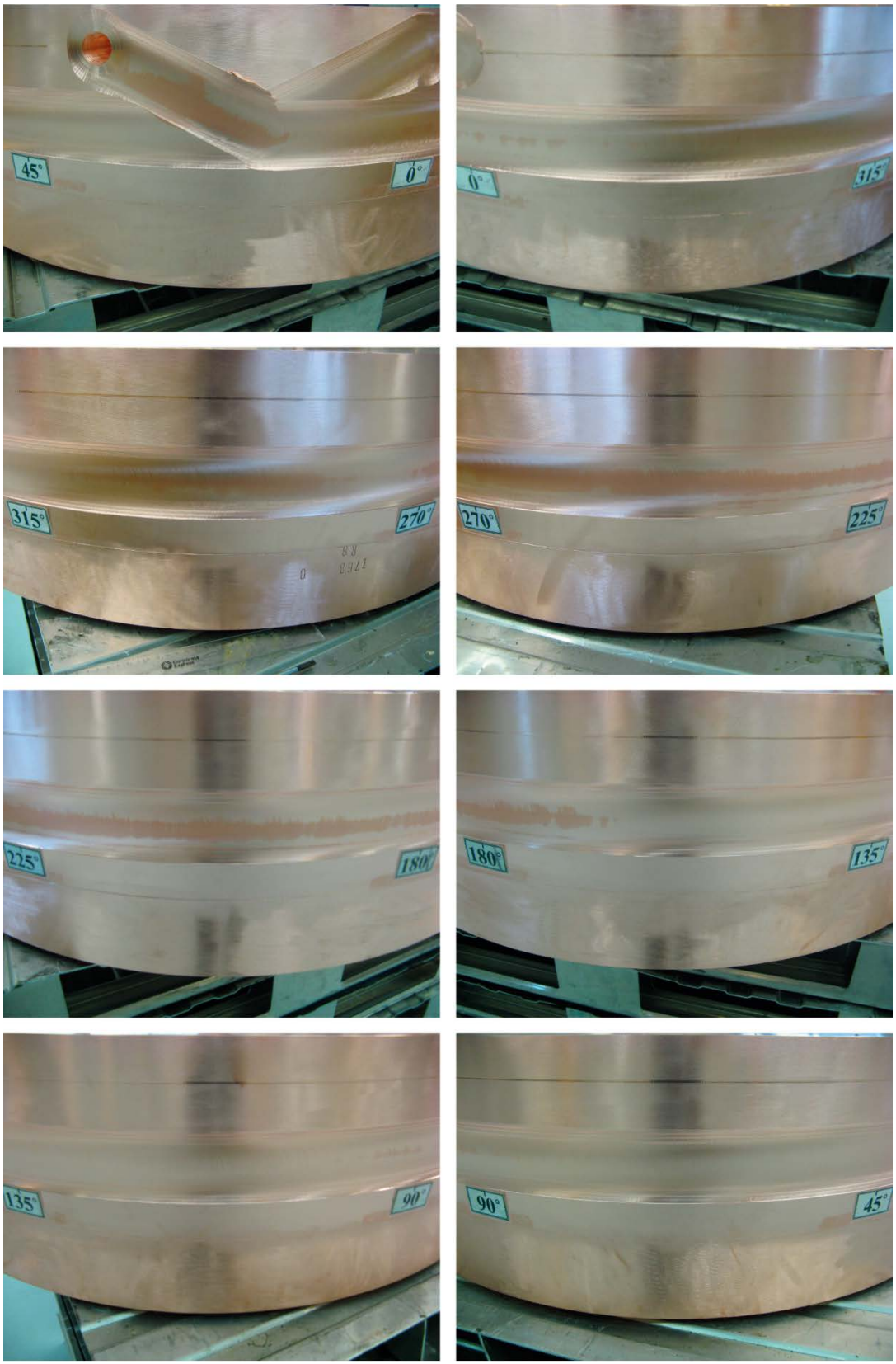

Figure 5-9. *Photographs of the weld with external and internal gas shielding (FSWL109). Note the slight discolouring at some locations on the weld surface. Oxide layer thickness of the darker patches is estimated to be below 15 nm based on the model presented in Chapter 4.*

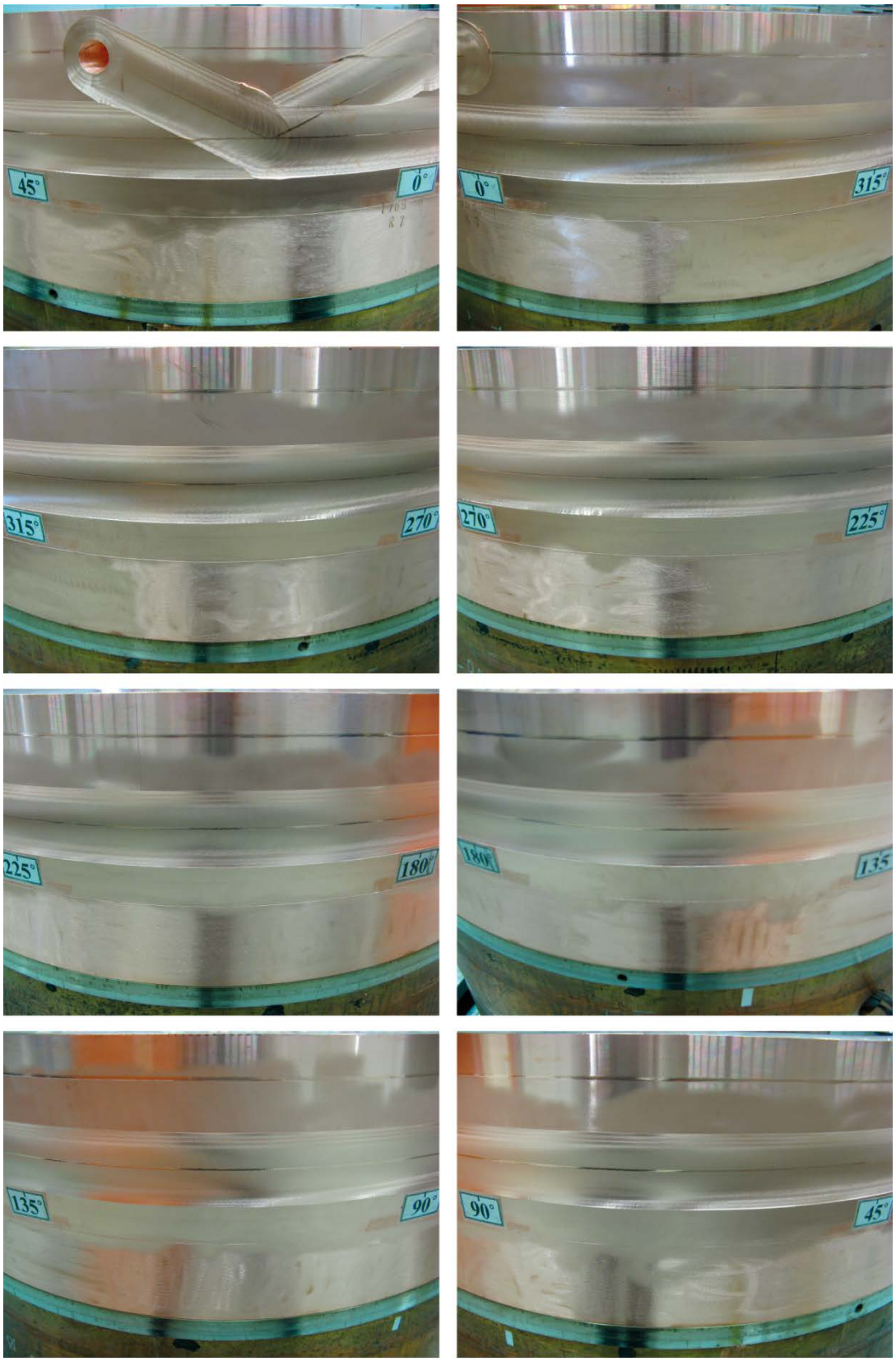

Figure 5-10. *Photographs of weld FSWL110 with external and internal hydrogen-containing shield gas. The shiny lines in the middle of the weld and at the top of the lid are from a ball bearing tool used to measure the position of the welded object after welding. No discolouring could be identified after welding which is interpreted as an oxide thickness below 5 nm, see text for details.*

5.2.2 Oxide particles embedded in weld

The extension of the oxide particle line from the root side (Figure 5-11) was measured from the electrolytically polished samples. The areas where the oxide particle line extends furthest into the weld region are located at an angular position of approximately 10°. At the overlap, at approximately 20°, the extension of the oxide line reaches a minimum. This indicates that more mixing occurred in the area that was travelled twice. In the weld with internal shielding gas, FSWL109, the oxide line extended shallower than FSWL108 with air on the root side. The larger extension of the oxide line for FSWL108 compared to FSWL109 is interpreted to be due to the internal gas shield of FSWL109 as the oxygen content in the external gas shield was, as can be seen in Figure 5-6, similar for both welds. This is most pronounced at 10° since the start and down travel sequence will heat the joint line and that area will be exposed to the environment until the end of the weld when it will be sealed. Figure 5-12 shows pictures of the weld cross sections with the largest amount of oxide inclusions. None of the samples showed a continuous line of oxides. The FSWL108-11° shows isolated particles, although in a streak. At the steady state, the line of particles is difficult to discriminate, the lower row in Figure 5-12.

In Figure 5-11, FSWL110 has the same oxide line extension at the lower angles as FSWL109 but becomes larger at higher angles. It is expected that amount of oxide particles to be lower in FSWL110 since the weld was done in a reducing atmosphere. The metallographic microscope pictures in Figure 5-14 explain this contradiction since the identified extension is higher but the amount of oxides is lower. Comparing the picture for FSWL110-173°, the amount of oxide particles close to the root is lower than that in FSWL109-179°.

The hydrogen annealing tests did not show any indication of hydrogen embrittlement (open grain boundaries) for any of the samples extracted from the three welds. The degree of copper oxide as determined by comparison to ASTM F68-10 was 1/C for all samples. This is the lowest level on the comparison scale and indicates a low level of oxides present in the material. The comparison chart judge the degree of oxides on a 5 grade scale where 5 contain the highest degree of oxide particles. The letter denotes where in the microstructure the oxides are located: A is cross grain, B is within grain and C is grain boundaries. Micrographs of the area close to the slit are shown in Figure 5-13, which represent the areas with the highest degree of oxide particles of the studied samples. Lines can be seen in the figures; however, no grain boundaries are forced apart. The sample welded without an internal shielding gas, FSWL108, had a higher degree of oxides than that with an internal shielding gas, FSWL109, as expected. For examples of hydrogen-annealed material that show susceptibility to hydrogen embrittlement, the reader is referred to Mattsson and Schückher (1958).

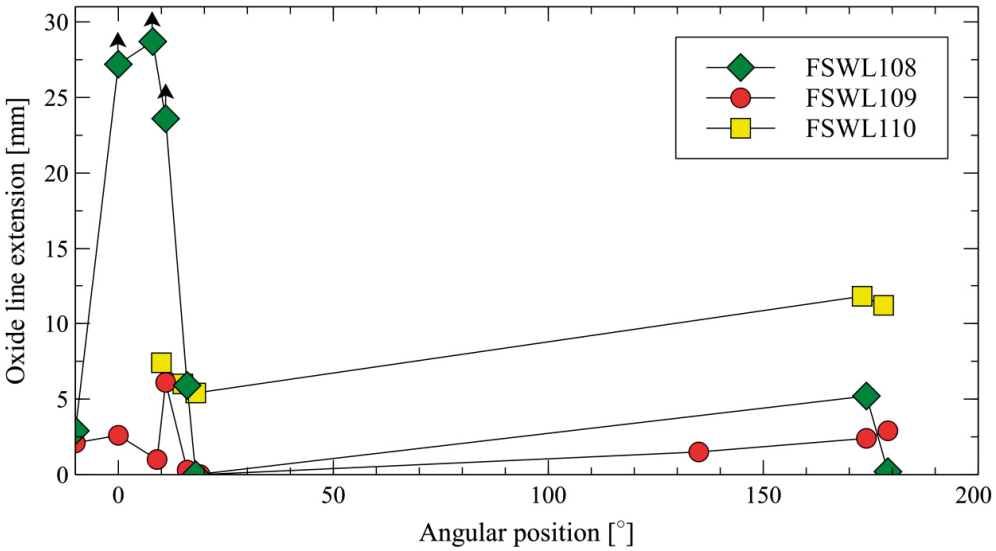

Figure 5-11. *The radial extension of the oxide line relative to the slit for the weld with only an external gas shield (green diamonds), the weld with external and internal gas shields (red circles) as well as the weld with internal and external gas shields containing hydrogen (yellow squares). The symbols marked with an arrow pointing upwards are a lower bound for the oxide line extension.*

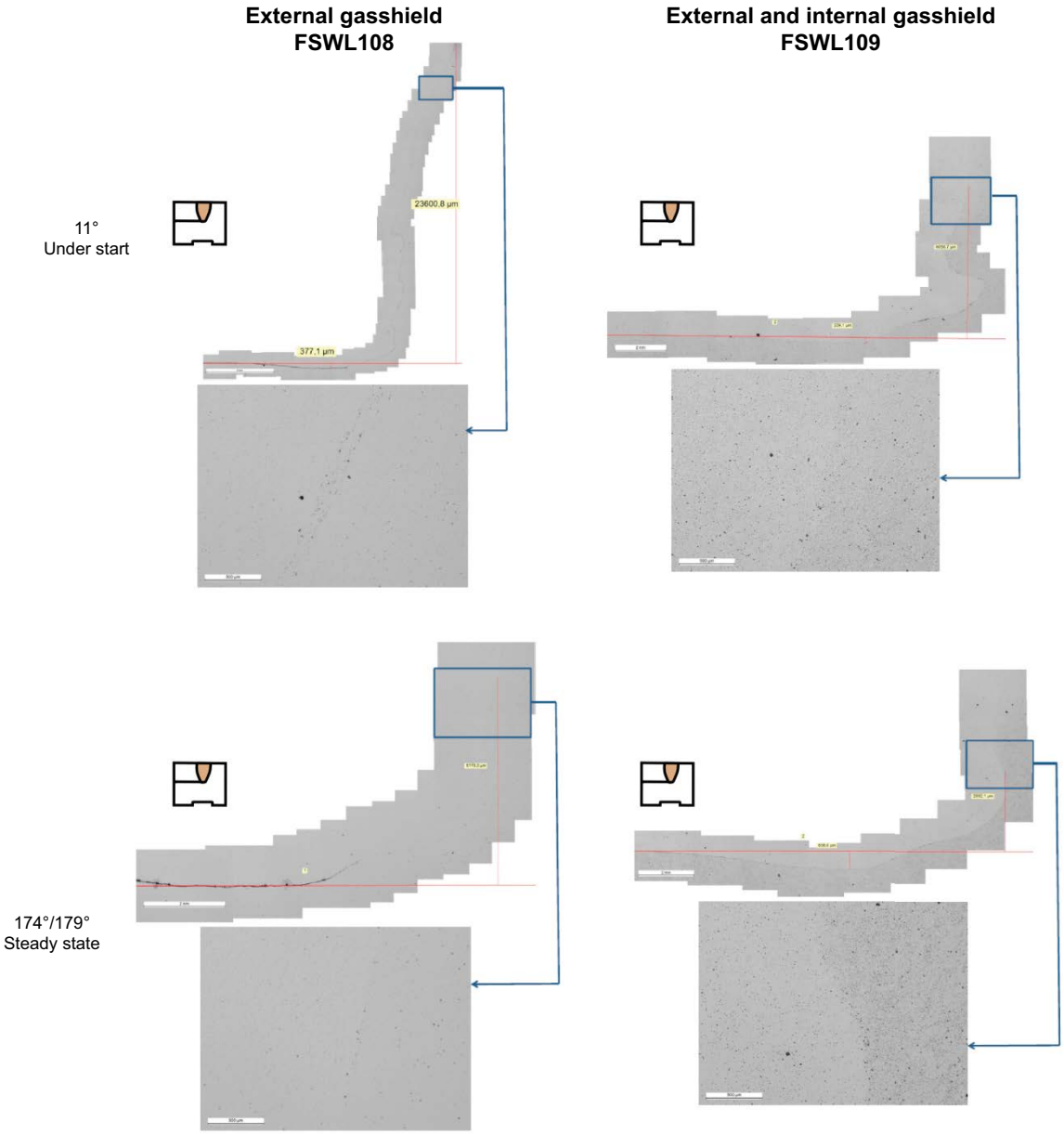

Figure 5-12. *Metallographic examination of the areas with the longest oxide line (top row) and the areas with longest oxide lines during steady state All metallographic pictures are taken at the root of the weld. The inset shows the orientation of the picture relative the weld (yellow), see Figure 5-5 for a full picture of a weld cross section.*

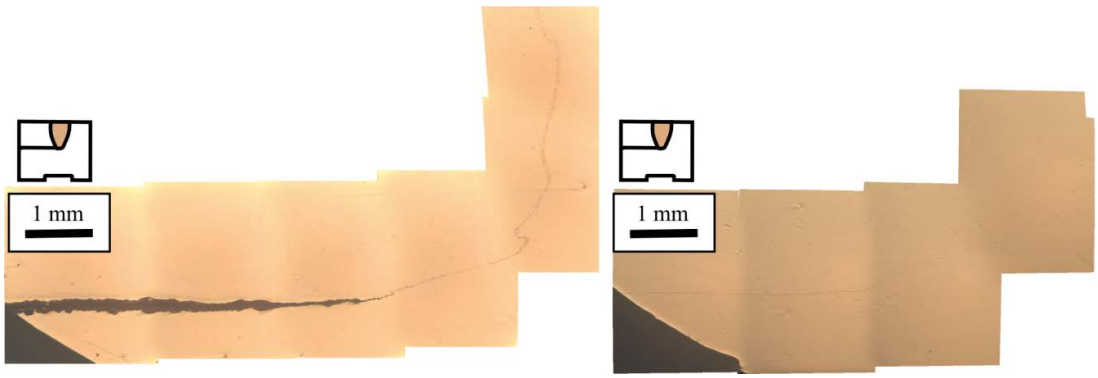

Figure 5-13. *Microscope pictures of the end of the slit for hydrogen-annealed samples FSWL108-18° (left) and FSWL109-19° (right). FSWL108 contains more oxide particles than FSWL109. The inset shows the orientation of the picture relative the weld (yellow). The inset shows the orientation of the picture relative the weld (yellow), see Figure 5-5 for a full picture of a weld cross section.*

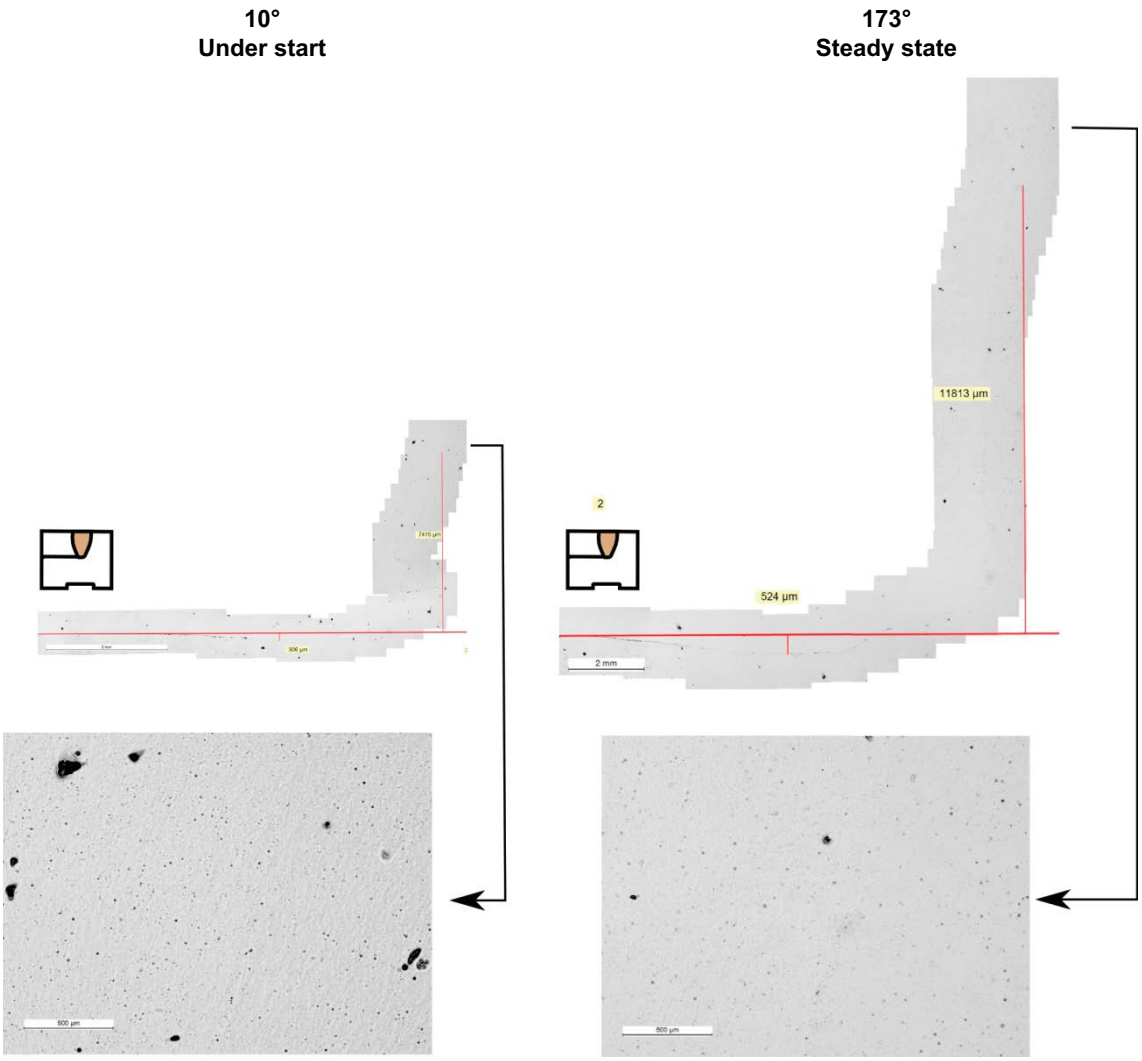

Figure 5-14. *Microscope pictures of the oxides close to the weld root for the weld prepared with a hydrogen-containing atmosphere (FSWL110). The inset shows the orientation of the picture relative the weld (yellow). The inset shows the orientation of the picture relative the weld (yellow), see Figure 5-5 for a full picture of a weld cross section.*

The oxygen content of the three welds is presented in Figure 5-15. All measurement points fall below 5 wt-ppm, which is the specification for the base material. The position FSWL108-12° has a slightly larger range than the remaining positions. The mean and standard deviations for the different cross sections are presented in Table 5-2. Due to the low number of measurements of the tube and lid, the mean and standard deviation are calculated for all objects. The measurement accuracy is 0.13, which is the same as the value obtained for the lid. All other rows in Table 5-2 have higher standard deviations, showing that the material has some intrinsic distribution. The highest mean value is 1.3 wt-ppm, and the highest standard deviation measured is 0.5 wt-ppm, which is 7 standard deviations from 5 wt-ppm.

Assuming that the material mixes completely during the FSW process, the total oxygen content for the welding zone should be the average of the lid and tube material, which is 1.2 ± 0.3 wt-ppm. If all samples from the lid and tube are merged into one single data set, then the average is 1.2 ± 0.5 wt-ppm. This would correspond to no mixing within the sampling volume of the measurement. The bimodal distribution of the oxygen content measurements for FSWL109 and FSWL110 seen in Figure 5-15 indicates that the mixing is not complete. The true process probably lies between these two limiting cases. In the remainder, we discuss the first case. All oxygen content measurements for FSWL109 and FSWL110 fall within two standard deviations, as shown in Figure 5-15. For FSWL108 is point is outside two standard deviations. With the available data and the accuracy of the experiment, welds FSWL109 and FSWL110 do not show increased oxygen content with respect to the base

material. These results do not contradict previous calculations (Björck 2015), which indicated that the increase in oxygen content in the weld material should be < 0.5 wt-ppm for a gas shield with an oxygen content < 50 at-ppm. This is of the same order of magnitude as the natural range between the tube and lid, as well as the accuracy of the measurement method itself. FSWL108-12° showed a slight difference compared to the other cross section. However, calculations assuming no gas shields indicate that the oxygen content should increase to a maximum value of 100 wt-ppm (Björck 2015). The fact that FSWL108-12° and FSWL108-175° has a comparable oxygen content as FSWL109 and FSWL110 indicates that the internal gas shield has a small effect. The geometry at the root side with a long slit coupled with the compressive forces on the joint line during welding most probably limit the availability of oxygen to the joint line from the inside. As the material will be heated up as the tool traverse down to the joint line the area probed in FSWL108-12° will be exposed to the environment longer than FSWL108-175°. This should produce a higher degree of oxidation (Björck 2015).

Table 5-2. The calculated mean and standard deviation for the different weld cross sections and the base material.

Description	Mean [wt-ppm]	Standard deviation [wt-ppm]
FSWL108-12	1.3	0.5
FSWL108-175	1.2	0.3
FSWL109-13	1.3	0.3
FSWL109-175	1.1	0.3
FSWL110-11	1.1	0.3
FSWL110-175	1.1	0.3
Lid	0.75	0.1
Tube	1.6	0.5
Lid + tube	1.2	0.5

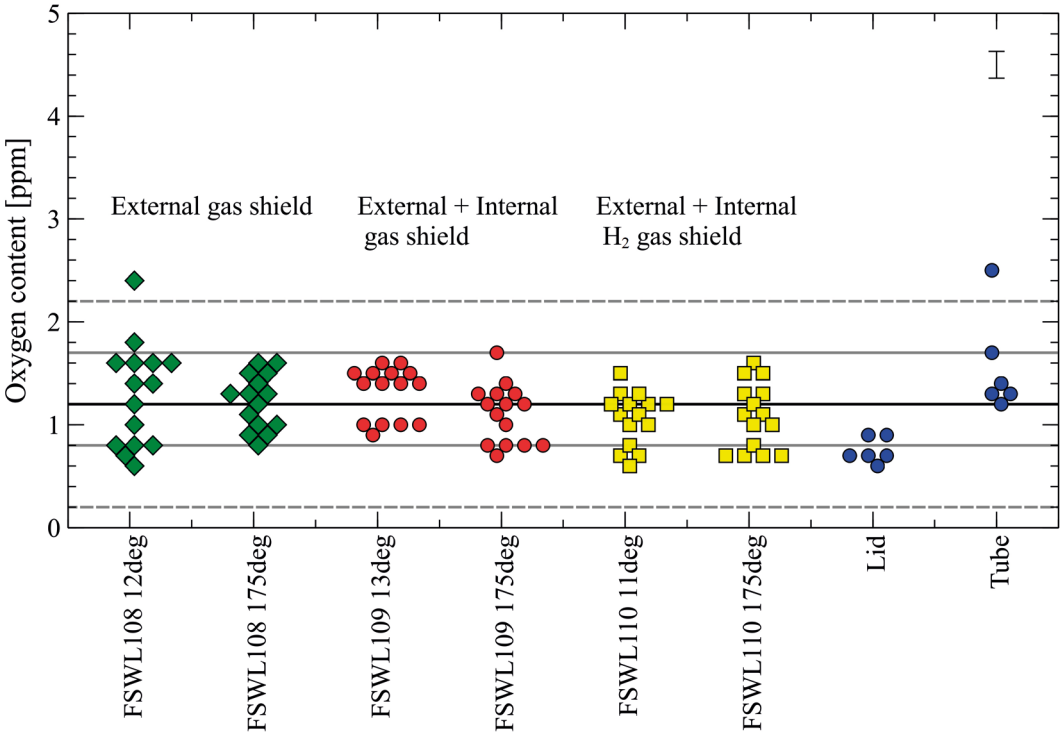

Figure 5-15. *The oxygen content measured for the weld with only an external gas shield (green diamonds), the weld with external and internal gas shields (red circles), the weld with external and internal gas shields containing hydrogen (yellow squares) and the base material (blue circles). The horizontal black line shows the mean of the lid and tube oxygen contents. The grey lines denote one standard deviation (full line) and two standard deviations (dashed lines). The measurement accuracy (1 standard deviation) of the measurements is indicated by the bar in the upper right corner.*

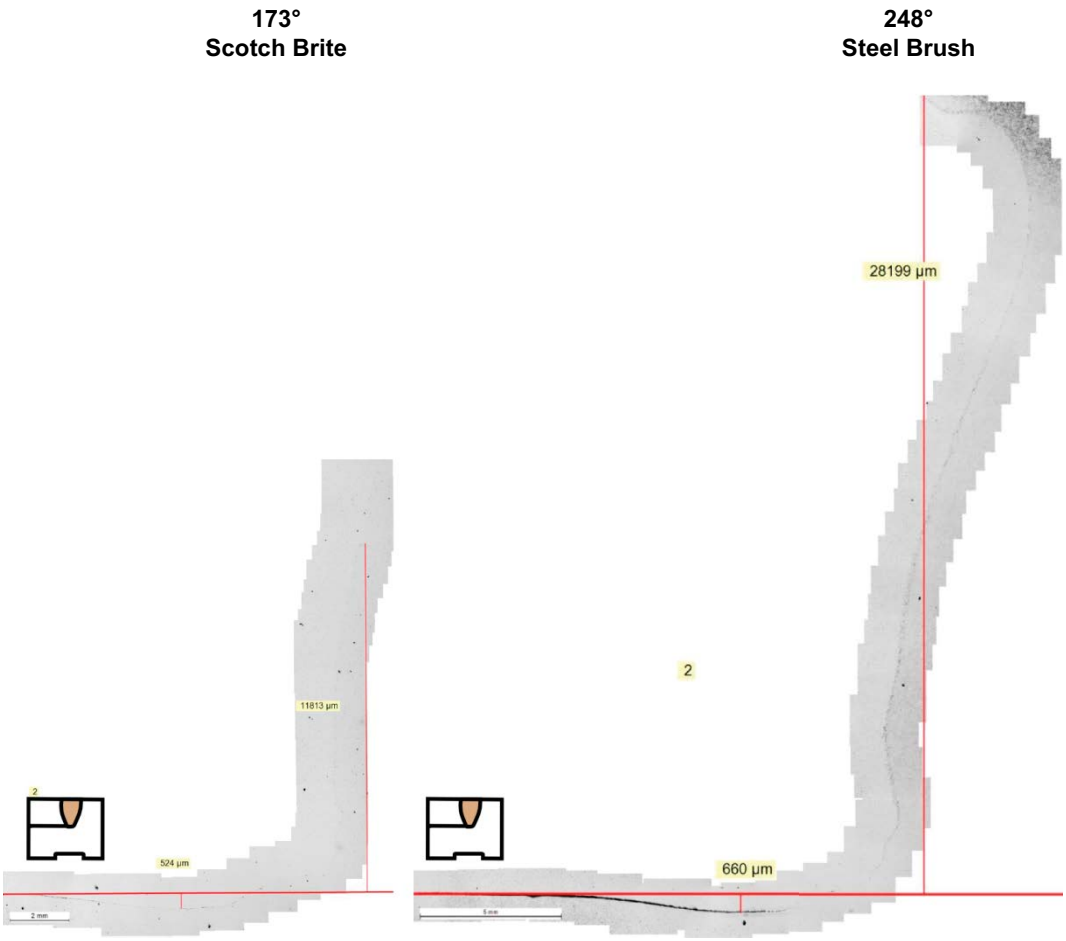

Figure 5-16. *Comparison of the area in FSWL110 at 180° that was cleaned with Scotch-Brite, left, and the area at 248° cleaned with the steel brush, right.*

5.2.3 Effect of cleaning method

The section of FSWL110 that was cleaned with a steel brush was investigated only with metallography of electrolytically polished samples. When cleaned, the Scotch Brite-cleaned surface shows a dull appearance, whereas the surface cleaned with a steel brush has a shinier appearance with a structure similar to an orange peel. The resulting oxide particle content after welding is shown in Figure 5-16. The part cleaned with a steel brush has a longer line of oxide inclusions than that cleaned with Scotch Brite, possibly due to the plastic deformation caused by the steel brush that most likely traps material by folding over the copper. The steel brush method is inferior to the Scotch Brite in cleaning the joint surfaces.

Because the mechanical steel brush leaves residues in the weld zone, it can be assumed that using a manual steel brush will cause the same effect. This could be a reason why a small amount of oxide particles can be found close to the weld root in the steady state samples. The inside corner of the lid is one of the parts where the steel brush is applied.

6 Summary and Conclusions

A new gas shield was implemented in the Canister Laboratory's FSW machine. Its performance was evaluated using full-size welds.

Different cleaning methods for preparing the joint surfaces were compared (CO_2 cleaning, laser cleaning, plasma cleaning, abrasive cleaning with a Scotch-Brite wheel and a rotating steel brush) using XPS. The abrasive cleaning method with a Scotch-Brite wheel was selected for the welding trials in this study. This method were judged to be simple to use for the trial welds and compared well with the other methods investigated with XPS.

The effect of shield gas on the inside was evaluated along with the effect of mixing in 2 at-% H_2 in the shielding gas. These welds were compared with a weld that only had an external shielding gas. The welds were evaluated regarding the oxygen content, and hydrogen annealing tests were conducted according to ASTM B577-16. In addition, the amount of oxide in the copper was evaluated by inspecting a metallographic cross section prepared with an electrolytic polishing procedure.

The results showed that none of the welds was susceptible to hydrogen embrittlement, and the copper oxide level was determined as 1/C according to the ASTM F68-10 comparison chart. The oxygen content of all welds were the same as those for the base material, and no increase of practical significance in the oxygen content compared to the base material could be found for the welds with an internal shielding gas. The weld without internal shielding gas had one of 15 measurement points that deviated by more than 2 standard deviations from the base material. All welds fulfilled the acceptance criteria for the base material of 5 wt-ppm O.

The weld conducted without internal gas shielding showed the largest amount of oxide inclusions that extended throughout the investigated area (26 mm radial extension) at the position before the tool reaches the joint line. This location is also where the other two welds had the highest degree of oxide particles, which agrees with previous theoretical considerations (Björck 2015). The other two welds showed a smaller amount of oxide inclusions. All investigated positions showed some residual oxide particles a few millimetres from the weld root. By comparing with a steel-brushed joint surface, this result was speculated to be because a steel brush was used to clean the lid corner at the weld root.

References

SKB's (Svensk Kärnbränslehantering AB) publications can be found at www.skb.com/publications.
SKBdoc-documents will be submitted upon request to document@skb.se.
Posiva's publications can be found at http://posiva.fi/en/databank.

Andrews R E, 2004. Friction stir welding – an alternative method for sealing nuclear waste storage canisters. SKB TR-04-16, Svensk Kärnbränslehantering AB.

ASTM B577-16. Standard test methods for the detection of cuprous oxide (hydrogen embrittlement susceptibility) in copper. West Conshohocken, PA: ASTM International.

ASTM F68-10. Standard specification for oxygen-free copper in wrought forms for electron devices. West Conshohocken, PA: ASTM International.

Babar S, Weaver J H, 2015. Optical constants of Cu, Ag, and Au revisited. Applied Optics 54, 477–481.

Björck M, 2013. FSWL94 – Measurement of temperatures and surrounding oxygen levels during welding. SKBdoc 1371191 ver 1.0, Svensk Kärnbränslehantering AB.

Björck M, 2015. Estimation of oxide growth on joint surfaces during FSW. SKBdoc 1402837 ver 1.0, Svensk Kärnbränslehantering AB.

Björck M, Elger R, 2013. Oxidation kinetics of copper at reduced oxygen partial pressures. SKBdoc 1410172 ver 1.0, Svensk Kärnbränslehantering AB.

Boman M, Ottoson M, Berger R, Andersson Y, Hahlin M, Björefors F, Gustafsson T, 2014. Corrosion of copper in ultrapure water. SKB R-14-07, Svensk Kärnbränslehantering AB.

Born M, Wolf E, 1992. Principles of optics: electromagnetic theory of propagation, interference and diffraction of light. Oxford: Pergamon.

Cederqvist L, 2014. Sealing of the canister. SKBdoc 1435653 ver 1.0, Svensk Kärnbränslehantering AB.

Chen H-B, Yan K, Lin T, Chen S-B, Jiang C-Y, Zhao Y, 2006. The investigation of typical welding defects for 5456 aluminum alloy friction stir welds. Materials Science and Engineering A 433, 64–69.

CIE, n d. CIE – International Commission on Illumination. Available at: http://www.cie.co.at [23 August 2017].

Ehrenreich H, Philipp H R, 1962. Optical properties of Ag and Cu. Physical Review 128, 1622–1629.

Hirsimäki M, Lampimäki M, Lahtonen K, Chorkendorff I, Valden M, 2005. Investigation of the role of oxygen induced segregation of Cu during Cu_2O formation on Cu{100}, Ag/Cu{100} and Cu(Ag) alloy. Surface Science 583, 157–165.

IEC 61966-2-1:1999. Multimedia systems and equipment – Colour measurement and management – Part 2-1: Colour management – Default RGB colour space – sRGB. Geneva: International Electrotechnical Commission.

Lantz K, 2015. Macro sample of FSW108 and FSW109. PRO15-1579, Exova AB. SKBdoc 1524247 ver 1.0, Svensk Kärnbränslehantering AB.

Lynch D W, Hunter W R, 1997. Comments on the optical constants of metals and an introduction to the data for several metals. In Palik E D (ed). Handbook of optical constants of solids. Burlington: Academic Press, 275–367.

Mattsson E, Schückher F, 1958. An investigation of hydrogen embrittlement in copper. Journal of the Institute of Metals 87, 241–247.

Pehkonen H, 2014. Design av gasskydd för friktionsomrörningssvetsningsmaskin. Master thesis. Deparment for econmical and industrial development, Linköping university. (LIU-IEI-TEK-A-14/01934-SE) (In Swedish.)

Parratt L G, 1954. Surface studies of solids by total reflection of x-rays. Physical Review 95, 359.

Purhonen T, 2014. State of the art of the welding method for sealing spent nuclear fuel canister made of copper. Part1 – FSW. Posiva Working Report 2014-22, Posiva Oy.

Rantala J, Auerkari P, Laukkanen A, Andersson T, Saukkonen T, 2015. Material integrity of welded copper overpack – Annual report 2014. Research Report VTT-R-00773-15, Technical Research Centre of Finland.

Reuterswärd H, Lantz K, 2015a. Macro sample of FSW108 and FSW109. PRO15-0901, Exova AB. SKBdoc 1491495 ver 2.0, Svensk Kärnbränslehantering AB.

Reuterswärd H, Lantz K, 2015b. Macro sample of FSW110. PRO15-1040, Exova AB. SKBdoc 1494040 ver 2.0, Svensk Kärnbränslehantering AB.

Ribbing C G, Roos A, 1997. Copper oxides (Cu2O, CuO). In Palik E D (ed). Handbook of optical constants of solids. Burlington: Academic Press, 875–882.

Savolainen K, 2012. Friction stir welding of copper and microstructure and properties of the welds. PhD thesis. Department of Engineering Design and Production, Aalto University.

Scheuerlein C, Taborelli M, 2006. The assessment of metal surface cleanliness by XPS. Applied Surface Science 252, 4279–4288.

SKB, 2010. Design, production and initial state of the canister. SKB TR-10-14, Svensk Kärnbränslehantering AB.

SS-EN 1321:1997. Destructive tests on welds in metallic material – Macroscopic and microscopic examination of welds. Stockholm: Swedish Standards Institute.

Zangwill A, 1988. Physics at surfaces. Cambridge: Cambridge University Press.

Zhou C, Yang X, Luan G, 2006. Effect of oxide array on the fatigue property of friction stir welds. Scripta Materialia 54, 1515–1520.

Appendix 1

Detailed results from the XPS analysis of the different samples

Reference samples

The relative elemental surface concentrations of the reference samples are listed in Table A1-1 in relative atomic percentages (at-%). In addition to C, O and Cu, only Si and Cl are observed on the as-received sample.

The as-received sample Pos #49 was investigated with XPS after 8–9 months of storage under dry, atmospheric conditions (LA = long ageing). The long-term storage does not appear to affect the elemental composition of the as-received samples. The as-received sample from the new batch (Pos #1N) was cleaner than the as-received sample from the old batch (Pos #1).

Table A1-1. Relative elemental surface concentration of the reference samples (at-%) rounded to the nearest integer.

Sample	C (at-%)	O (at-%)	Cu (at-%)	Si (at-%)	Cl (at-%)
Pos #1 as-received	77	16	2	4	1
Pos #1 sputter cleaned	3	–	97	–	–
Pos #1 air oxidized	18	17	65	–	–
Pos #50 as-received (DP)	72	21	4	3	–
Pos #49 as-received (LA) Spot 1	69	25	5	1	0
Pos #49 as-received ((LA) Spot 2	71	22	5	1	1
Pos #1N as-received (new batch)	60	24	16	–	–

DP = depth profiling. LA = long ageing.

The chemical states of C, O and Cu are listed in Table A1-2 for the reference samples. The silicon observed on the as-received sample originates from Si^{4+} (possibly SiO_2). The chemical state of chlorine is Cl^- for all samples. During long-term storage, Cu oxidation occurred.

Table A1-2. Relative elemental specific chemical states (%) of the reference samples rounded to the nearest integer.

Sample	C 1s (% of C)			O 1s (% of O)		Cu LMM (% of Cu)		
	C–C/H	C–O	(O–)C=O	O–Cu	O–C/=C	Cu^0	Cu^+	Cu^{2+}
Pos #1 as-received	81	15	4	19	81	16	74	10
Pos #1 sputter cleaned	100	–	–	–	–	93	7	–
Pos #1 air oxidized	85	1	15	76	24	47	35	19
Pos #50 as-received (DP)	76	18	6	9	91	7	54	38
Pos #49 as-received (LA) Spot 1	62	23	15	84	16	5	28	56
Pos #49 as-received (LA) Spot 2	63	22	16	87	13	7	45	48
Pos #1N as-received (new patch)	84	9	6	70	30	22	57	21

DP = depth profile. LA = long ageing.

Depth profiling was performed for the as-received Pos #50 sample. The relative elemental surface concentrations as a function of the sputtering time are shown in Figure A1-1. Trace amounts of Zn and Cl were observed after 6 s of sputtering, but not before or after. The oxygen was removed after 42 s of sputtering, whereas some carbon remained after 300 s.

Figure A1-2 shows the changes in the chemical states of Cu. The as-received sample represents the oxidation stage before the cleaning procedures. The copper oxide layer consists mostly of Cu_2O. CuO is observed in the outermost oxide layer.

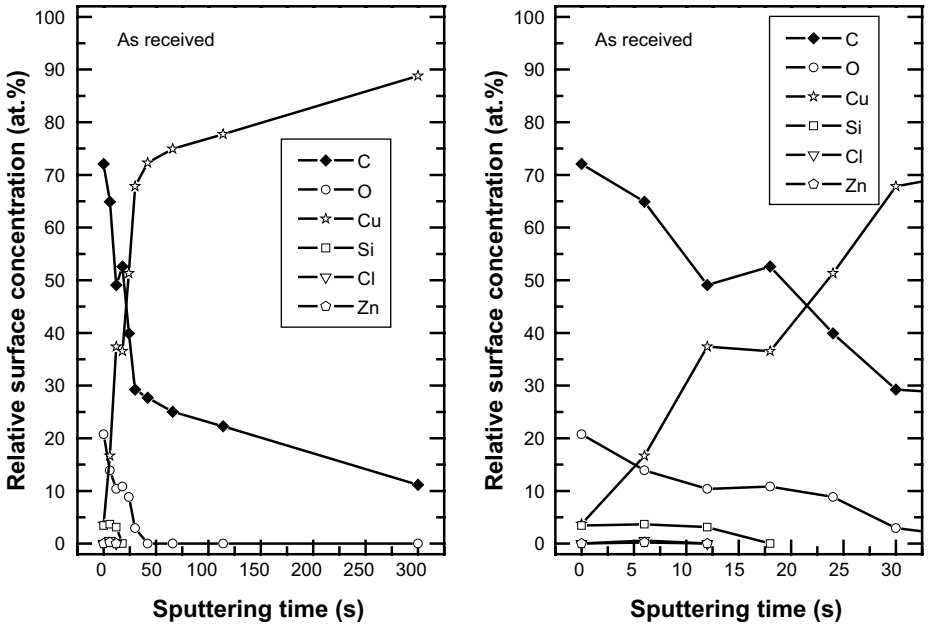

Figure A1-1. *Depth profiling of the Pos #50 as-received sample. The figure on the right shows the initial stages of the depth profiling.*

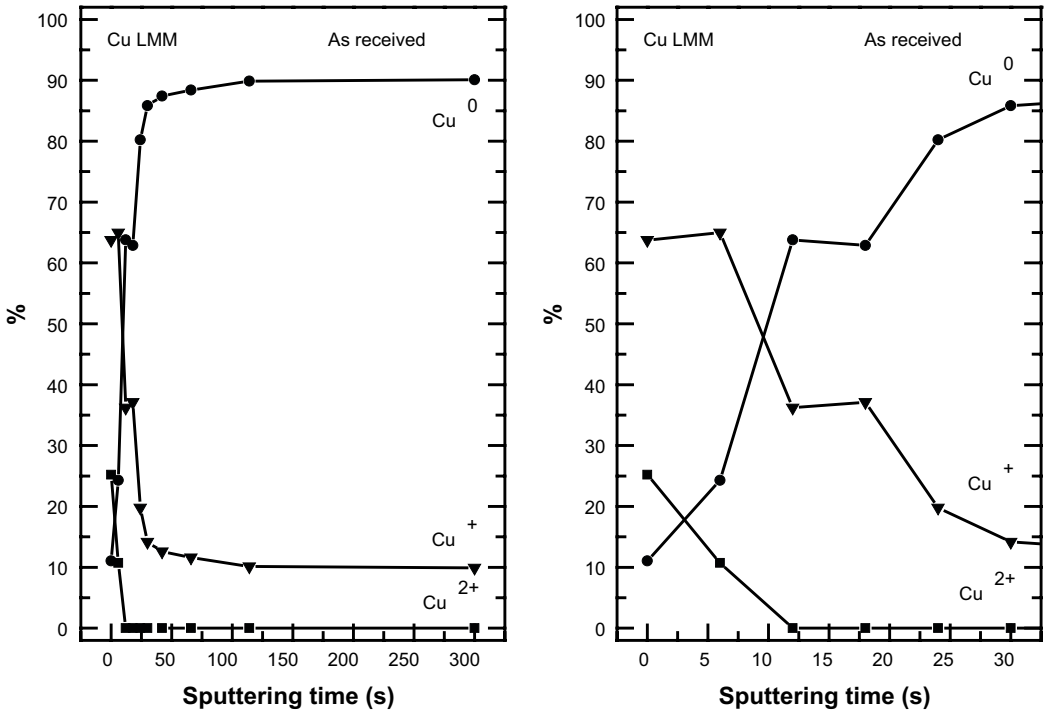

Figure A1-2. *Changes in the chemical states of Cu during depth profiling of the as-received sample Pos#50. The figure on the right illustrates the initial stages of depth profiling.*

Abrasive cleaning

The relative elemental surface concentrations are listed in Table A1-3 in atomic percentages (at-%). Si is removed during abrasive cleaning. No new elements compared to the references are observed. The C impurity level is approximately double compared to the air-exposed reference. The relative surface concentration of C and O increased upon short and long ageing durations. A trace amount of S was observed locally after long ageing.

Table A1-3. Relative elemental surface concentration of the abrasively cleaned samples (at-%).

Sample	C (at-%)	O (at-%)	Cu (at-%)	Cl (at-%)	S(at-%)
Pos #33 Spot 1	40	22	36	2	–
Pos #33 Spot 2	37	20	42	2	–
Pos #34 (DP) Spot 1	44	26	29	1	–
Pos #34 (DP) Spot 2	42	21	36	1	–
Pos #21 (CF) Spot 1	41	21	36	2	–
Pos #35 (aged) Spot 1	52	31	16	2	–
Pos #35 (aged) Spot 2	52	28	19	1	–
Pos #36 (LA) Spot 1	63	29	8	–	–
Pos #36 (LA) Spot 2	60	23	15	0	1

DP = depth profiling, LA = long ageing, CF = cutting fluids.

The chemical compositions of C, O and Cu in the samples are listed in Table A1-4. The chemical state of chlorine is Cl^- for all samples. The relatively high percentage of metallic Cu indicates the presence of a thin copper oxide layer. During ageing (two weeks and long ageing), more organic impurities are accumulated at the surface, and the copper is oxidized further.

Table A1-4. Relative elemental specific chemical states (%) of the abrasively cleaned samples.

Sample	C 1s (% of C)			O 1s (% of O)		Cu LMM (% of Cu)		
	C–C/H	C–O	(O–)C=O	O–Cu	O–C/=C	Cu^0	Cu^+	Cu^{2+}
Pos #33 Spot 1	66	22	12	70	30	41	42	17
Pos #33 Spot 2	74	17	10	75	25	43	46	11
Pos #34 (DP) Spot 1	70	19	12	69	31	35	41	24
Pos #34 (DP) Spot 2	73	17	10	71	29	37	50	13
Pos #21 (CF) Spot 1	68	21	11	70	30	43	40	17
Pos #35 (aged) Spot 1	64	17	18	66	34	28	56	16
Pos #35 (aged) Spot 2	70	15	15	66	35	29	63	8
Pos #36 (LA) Spot 1	71	15	14	89	11	11	62	27
Pos #36 (LA) Spot 2	75	13	12	60	40	17	79	3

DP = depth profiling, LA = long ageing, CF = cutting fluids.

Depth profiling was performed for Pos #34. The relative elemental surface concentrations as a function of the sputtering time are shown in Figure A1-3. The oxygen was removed after 21 s of sputtering. Thus, the thickness of the overlayer including surface impurities and the oxide layer on the abrasively cleaned sample is approximately 50 % of that of the overlayer on the as-received reference sample.

Chlorine is only observed in the overlayer of impurities with very small amounts. The amount of CuO is lower in the outermost copper oxide layer than on the as-received sample and is rapidly removed during the depth profiling (Figure A1-4).

CO_2 cleaning

The CO_2-cleaned samples have relative surface concentrations of C, O and Cu, see Table A1-5, similar to those of the mechanically cleaned samples, but the amount of the other impurities is higher. Si was observed on two samples, whereas Cl and S were observed on all samples. The aged sample contained fluorine. The variations in the relative surface concentrations between samples and different analysis locations on the samples are larger than on the mechanically cleaned samples.

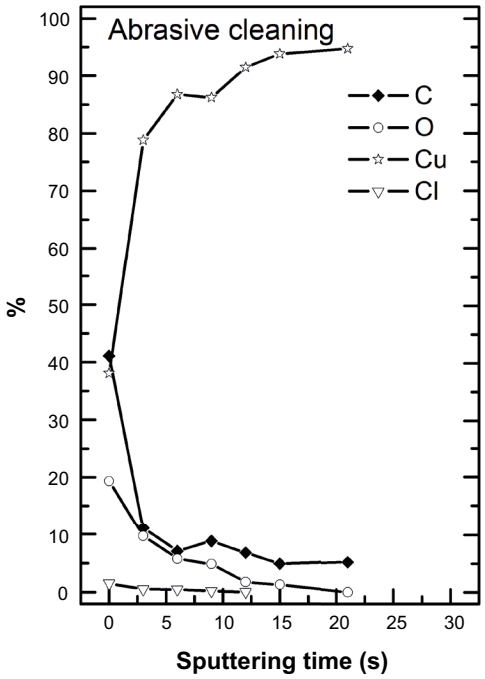

Figure A1-3. *Depth profiling for abrasively cleaned sample Pos #34.*

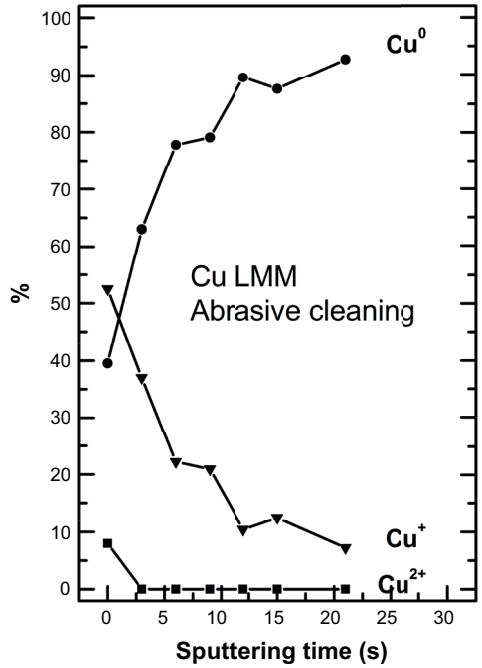

Figure A1-4. *Changes in the chemical states of Cu during depth profiling of the mechanically cleaned sample Pos#34.*

Table A1-5. Relative elemental surface concentration of the reference samples (at-%).

Sample	C (at-%)	O (at-%)	Cu (at-%)	Si (at-%)	Cl (at-%)	S (at-%)	F(at-%)
Pos #9	40	19	30	2	2	7	–
Pos #11 (DP)	32	23	39	–	3	4	–
Pos #17 (CF) Spot 1	33	27	33	–	3	3	–
Pos #17 (CF) Spot 2	33	20	39	–	3	5	–
Pos #11 (aged) Spot 1	36	33	20	4	1	3	2
Pos #11 (aged) Spot 2	31	32	27	2	1	3	4

DP = depth profiling, LA = long ageing, CF = cutting fluids.

The chemical state of the silicon is Si^{4+} (possibly SiO_2). The chemical state of the chlorine is Cl^- for all samples. The chemical state of the sulphur is S^0/S^{2-}. The chemical states of C, O and Cu are presented in Table A1-6. CuO is observed only in the aged samples. The low temperature of the samples during the cleaning procedure may inhibit CuO formation.

Table A1-6. Relative elemental specific chemical states (%) of the CO_2-cleaned samples.

Sample	C 1 s (% of C)			O 1 s (% of O)		Cu LMM (% of Cu)		
	C–C/H	C–O	(O–)C=O	O–Cu	O–C/=C	Cu^0	Cu^+	Cu^{2+}
Pos #9	83	13	4	66	35	15	85	–
Pos #11 (DP)	73	18	9	75	25	19	81	–
Pos #17 (CF) Spot 1	67	21	12	65	35	21	79	–
Pos #17 (CF) Spot 2	68	21	11	72	28	21	79	–
Pos #10 (aged) Spot 1	74	11	14	45	55	9	83	9
Pos #10 (aged) Spot 2	72	11	16	58	42	8	83	10

Figure A1-5 show the depth profiling of CO_2-cleaned sample Pos #11. Oxygen is removed after 15 s, which indicates that the thickness of the surface layer including impurities and the oxides is similar to that of the mechanically cleaned samples. The changes in the Cu oxidation state during depth profiling are shown in Figure A1-6.

Laser cleaning

The relative elemental surface concentrations of laser-cleaned samples are shown in Table A1-7. The level of C and O is similar to that in the air-exposed samples and was even lower on some samples. Note also that a part of the sample surface was visibly dark (Figure A1-7). The dark areas were measured on samples Pos #32 Spot 2 and on Pos #31 (aged) Spot 2. On both of these samples, the dark area was significantly more oxidized than the lighter areas.

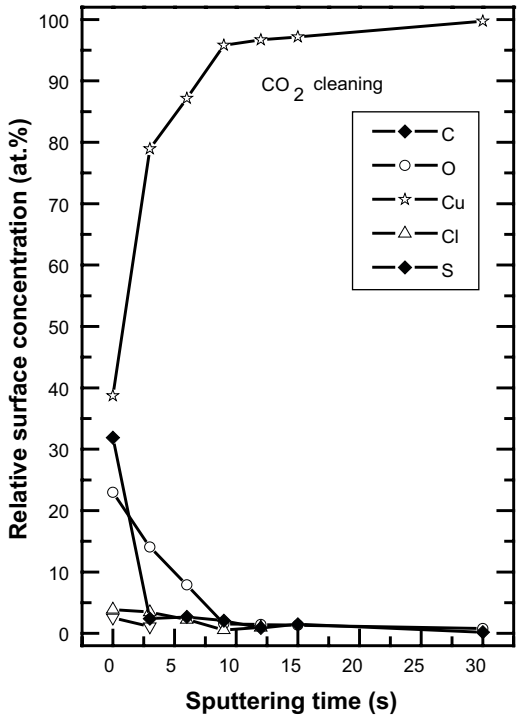

Figure A1-5. *Depth profiling for CO_2-cleaned sample Pos #11.*

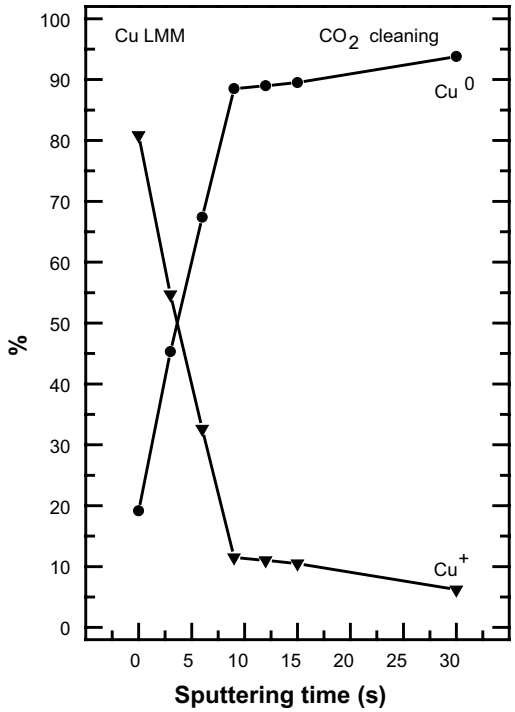

Figure A1-6. *Changes in the chemical states of Cu during depth profiling of the CO_2-cleaned sample Pos#11.*

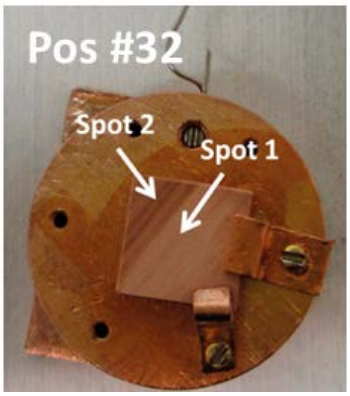

Figure A1-7. *Sample Pos #32 in the sample holder. The approximate areas of measuring spots 1 and 2 are indicated.*

Table A1-7. Table 5.5.1. Relative elemental surface concentration of the laser-cleaned samples (at-%).

Sample	C (at-%)	O (at-%)	Cu (at-%)	Si (at-%)	Cl (at-%)
Pos #28 Spot 1	18	31	51	–	–
Pos #28 Spot 2	19	23	60	–	–
Pos #32 (DP) Spot 1 (light)	14	29	57	–	–
Pos #32 (DP) Spot 2 (dark)	16	43	40	–	–
Pos #18 (CF) Spot 1	13	31	56	–	–
Pos #18 (CF) Spot 2	14	31	55	–	–
Pos #31 aged Spot 1(light)	27	41	29	2	1
Pos #31 aged Spot 2 (dark)	63	24	9	4	–

DP = depth profiling, CF = cutting fluids.

The chemical compositions of C, O and Cu of the laser-cleaned samples are shown in Table A1-8. A comparison of the light and dark areas on the samples shows significant differences in the oxidation state. The dark areas have a high percentage of CuO and a low percentage of metallic Cu, whereas on light areas, the situation is opposite. This indicates that the oxide layer thickness varies across the sample. With other cleaning methods, these variations are not observed. The dark areas also accumulate more carbon impurities during ageing than the light areas.

Table A1-8. Relative elemental specific chemical states (%) of the laser-cleaned samples.

Sample	C 1s (% of C)			O 1s (% of O)		Cu LMM (% of Cu)		
	C–C/H	C–O	(O–)C=O	O–Cu	O–C/=C	Cu^0	Cu^+	Cu^{2+}
Pos #28 Spot 1	79	9	24	76	24	17	71	12
Pos #28 Spot 2	84	5	11	76	24	19	72	10
Pos #32 (DP) Spot 1 (light)	91	–	9	76	24	22	65	13
Pos #32 (DP) Spot 2 (dark)	76	4	20	56	44	2	56	42
Pos #18 (CF) Spot 1	83	0	17	71	29	19	63	19
Pos #18 (CF) Spot 2	53	21	27	75	25	16	73	10
Pos #31 aged Spot 1 (light)	34	12	21	44	56	11	58	31
Pos #31 aged Spot 2 (dark)	87	6	6	31	69	–	45	54

Figure A1-8 shows the results of the depth profiling of the laser-cleaned sample. The depth profiling was performed on the light area of the sample (Spot 1). Although the initial relative surface concentration of O was similar to those of mechanical and CO_2 cleaning, the oxygen was not completely removed, even after 300 s of sputtering. Figure A1-9 shows the evolution of the copper chemical state during sputtering.

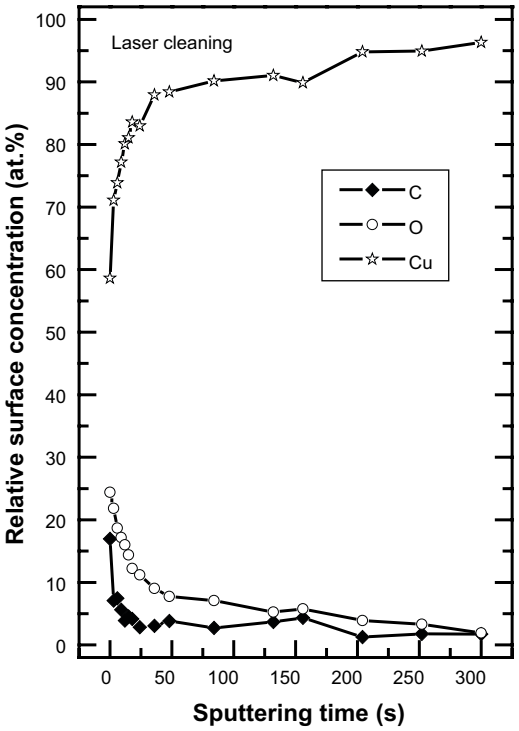

Figure A1-8. *Depth profiling for laser cleaned sample.*

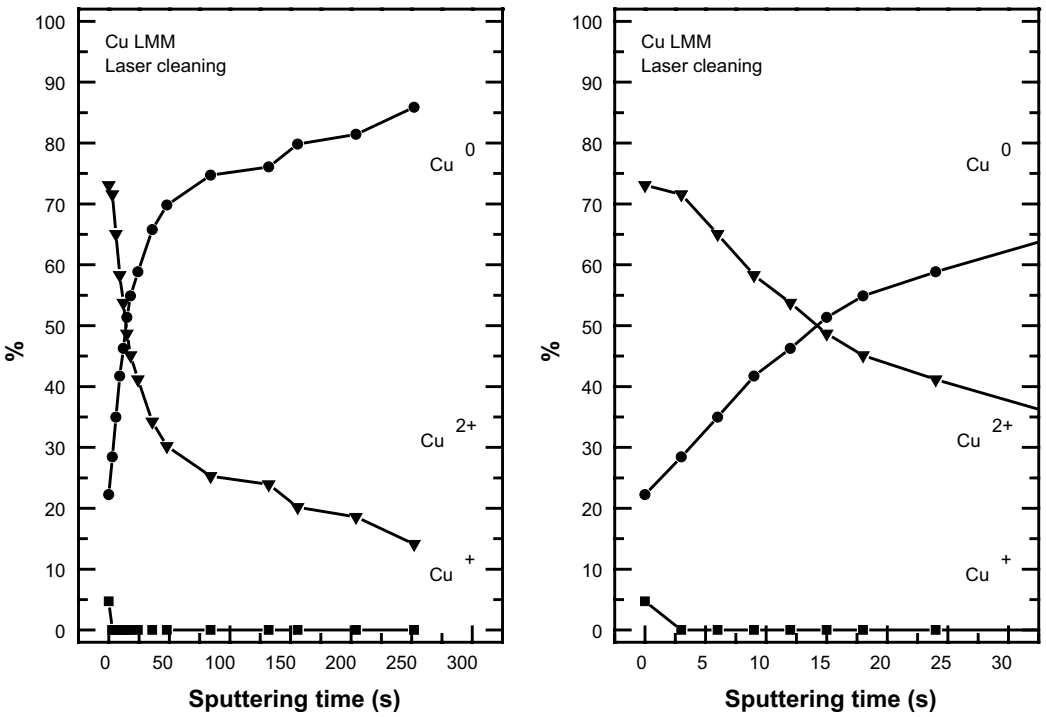

Figure A1-9. *The changes in the chemical states of Cu during depth profiling of the laser-cleaned sample Pos#32. The figure on the right illustrates the initial stages of depth profiling.*

Plasma cleaning

XPS was performed on three samples with different cleaning parameters, Pos #43 (air), Pos #44 (Formier 5) and Pos #45 (air, double cleaning time), and the last parameters were chosen for the remaining samples. The relative elemental surface concentrations are listed in Table A1-9 in atomic percentages (at-%). With plasma cleaning, the relative concentration of oxygen is the highest of all the methods. A doubled cleaning time reduces the amount of carbon to a level similar to the other methods. New impurities are observed on the plasma-cleaned samples. In addition to Si, Cl and S, which were observed with other cleaning methods, Zn, Fe and N were observed after plasma cleaning.

Table A1-9. Relative elemental surface concentration of the reference samples (at-%).

Sample	C (at-%)	O (at-%)	Cu (at-%)	Si (at-%)	Cl (at-%)	S (at-%)	Zn (at-%)	Fe (at-%)	N (at-%)
Pos #43 Spot 1	34	49	12	4	–	–	0	–	–
Pos #43 Spot 2	36	44	13	4	1	1	0	–	–
Pos #44 Spot 1	28	49	11	2	–	1	0	–	9
Pos #45 Spot 1	17	53	18	3	0	1	1	–	6
Pos #45 Spot 2	22	44	18	4	0	1	0	4	6
Pos #46 Spot 1	22	49	15	4	-	1	0	4	5
Pos #20 (CF) Spot 1	20	48	13	5	0	1	0	4	8
Pos #49 aged Spot 1	32	43	10	4	0	0	–	5	4
Pos #49 aged Spot 2	34	43	12	3	1	1	–	4	3

CF = cutting fluids.

The chemical composition of plasma-cleaned samples (as shown in Table A1-10) is significantly different from the other cleaning methods. First, the chemical states of C and O differ from the other cleaning methods and reference samples. This may be an indication of plasma-induced chemical reactions of C and O at the surface. Second, the copper is strongly oxidized, with a very high amount of CuO at the outermost oxide layer.

Table A1-10. Relative elemental specific chemical states (%) of the plasma-cleaned samples.

Sample	C 1s (% of C)			O 1s (% of O)		Cu LMM (% of Cu)		
	C–C/H	C–O	(O–)C=O	O–Cu	O–C/=C	Cu0	Cu^{+}	Cu^{2+}
Pos #43 Spot 1	64	21	14	17	83	–	34	66
Pos #43 Spot 2	63	23	15	22	78	–	35	65
Pos #44 Spot 1	69	18	12	9	91	4	42	54
Pos #45 Spot 1	61	20	19	41	59	–	25	75
Pos #45 Spot 2	63	18	17	49	51	–	26	73
Pos #46 Spot 1 (DP)	48	24	19	33	67	–	35	65
Pos #20 (CF) Spot 1	59	21	20	32	68	–	40	60
Pos #49 aged Spot 1	61	23	16	41	59	–	29	71
Pos #49 aged Spot 2	62	22	6	44	55	–	32	68

DP = depth profiling, CF = cutting fluids.

The results of the depth profile of plasma-cleaned samples are shown in Figure A1-10. The oxygen is removed after 160 s of sputtering, while a large amount of carbon remains. The depth profiling indicates that some impurities, such as Fe, Zn and N, may be implanted in the oxide layer. Figure A1-11 shows the changes in the chemical states of Cu during the depth profiling.

Stainless steel brush cleaning

The relative elemental surface concentrations of the samples cleaned with a stainless steel brush are listed in the Table A1-11 in atomic percentages (at-%). The observed elements are the same as those in abrasive cleaning, but the amount of C impurities is significantly higher. With other cleaning methods, the samples prepared with cutting fluids were very similar to samples without cutting fluids. On stainless steel brush-cleaned samples, the amount of C impurities is higher than on samples cut with the cutting fluids than on samples without the cutting fluids.

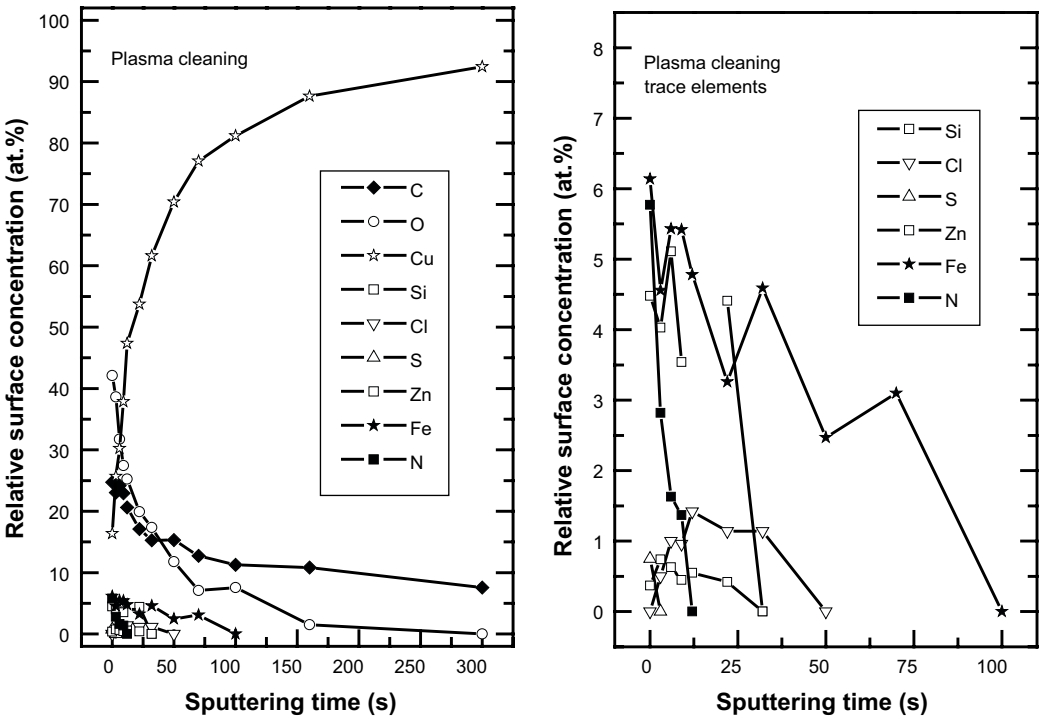

Figure A1-10. *Depth profiling of plasma-cleaned sample Pos#46. The figure on the right illustrates the relative surface concentrations of trace elements in the initial stages of the depth profile.*

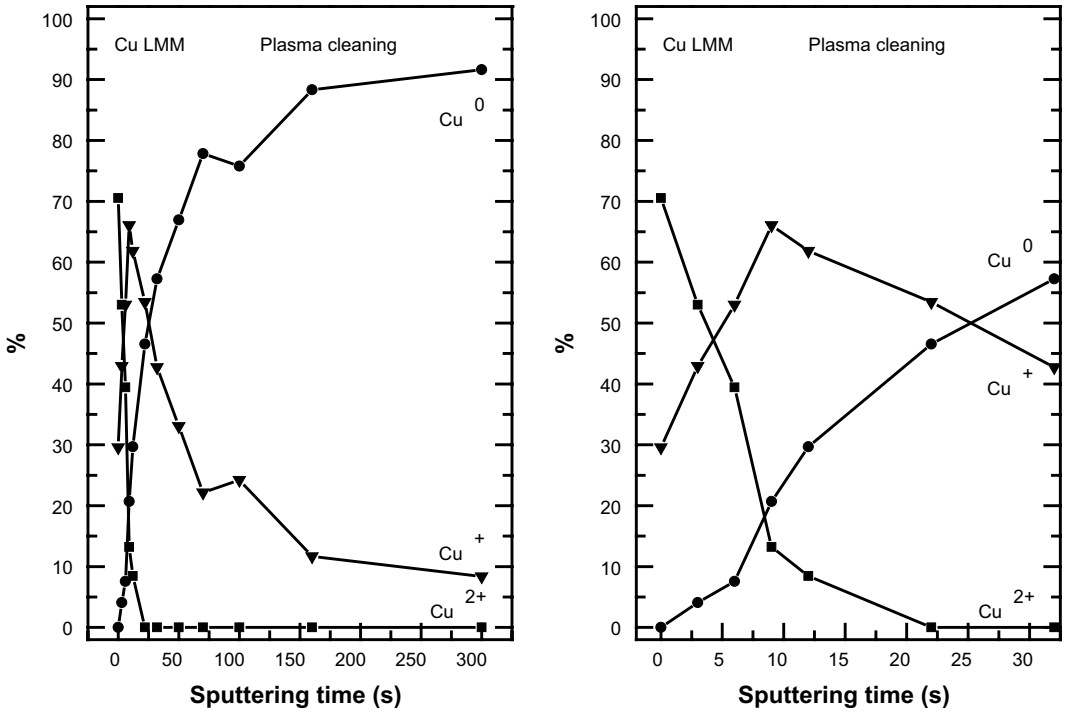

Figure A1-11. *Changes in the chemical states of Cu during depth profiling of the plasma-cleaned sample Pos#46. The figure on the right illustrates the initial stages of depth profiling.*

Table A1-11. Relative elemental surface concentration of the stainless steel brush-cleaned samples (at-%).

Sample	C (at-%)	O (at-%)	Cu (at-%)	Cl (at-%)
Pos #4N Spot 1	59	29	11	1
Pos #4N Spot 2	54	24	21	1
Pos #5N Spot 5 (DP)	62	25	12	0
Pos #11N (CF) Spot 1	76	20	3	0
Pos #11N (CF) Spot 1	79	15	5	0
Pos #6N (aged) Spot 1	67	28	4	0
Pos #6N (aged) Spot 2	63	25	11	1

DP = depth profiling, CF = sample prepared with cutting fluids.

The chemical compositions of C, O and Cu of the samples cleaned with stainless steel brush are listed in Table A1-12. The chemical state of the chlorine is Cl^- for all samples. A new chemical state of oxygen is observed in all steel brush-cleaned samples. The binding energy of the sample is ~534 eV, which indicates that it may originate from organic compounds containing C(O)=O or -C(O)O(O)C- groups or H_2O. This is in accordance with the higher relative surface concentrations of C on the stainless steel brushed samples compared to other methods and the chemical states of C. The result indicates that a new type of organic impurity is introduced to the surface upon stainless steel brush cleaning that differs from the typical atmospheric impurities observed on the other samples that have been exposed to air.

Table A1-12. Relative elemental specific chemical states (%) of the stainless steel brush-cleaned samples.

Sample	C 1s (% of C)			O 1s (% of O)			Cu LMM (% of Cu)		
	C–C/H	C–O	C(O)O(O)C-, (O–)C=O	O–Cu	O–C/=C	C(O)O(O)C- -C(O)=O, H_2O	Cu^0	Cu^+	Cu^{2+}
Pos #4N Spot 1	58	22	19	27	39	34	32	57	5
Pos #4N Spot 2	69	17	14	50	28	22	37	56	6
Pos #5N Spot 5 (DP)	65	21	15	33	35	31	36	50	14
Pos #11N (CF) Spot 1	71	17	11	21	45	35	40	52	7
Pos #11N (CF) Spot 1	79	14	7	34	35	31	42	41	18
Pos #6N (aged) Spot 1	64	21	15	25	42	33	21	70	9
Pos #6N (aged) Spot 2	71	15	14	44	37	20	24	76	–

DP = depth profiling, CF = cutting fluids.

Depth profiling was performed for the Pos #5N sample. The depth profile was performed with an Ar^+ sputtering gun with a sputtering speed of 0.031 nm/s, which is approximately 50% slower than the sputtering gun used in the other depth profiles. Additionally, the XPS analysis during the depth profile was performed with a different energy analyser than that used on the other samples. This is because the energy analyser was updated at the Surface Science Laboratory during the spring of 2015. The detection area for the XPS experiments of sample Pos #5N has a diameter of 1.93 mm.

The relative elemental surface concentrations as a function of the sputtering time are shown in Table A1-12. The oxygen was removed after 12 s of sputtering. Thus, considering the differences in the sputtering speed, the overlayer thickness including surface impurities and the oxide layer is similar to abrasive cleaning and CO_2 cleaning.

The amount of CuO is lower in the outermost copper oxide layer than on the as-received sample and is rapidly removed during the depth profiling (Figure A1-12), which is similar to abrasive cleaning.

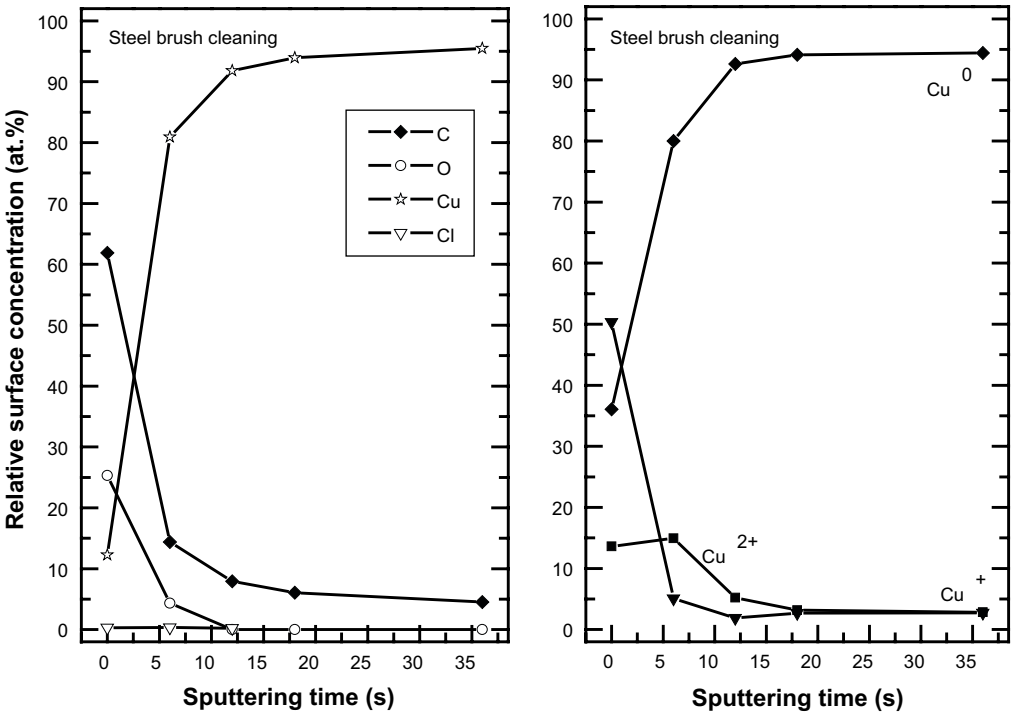

Figure A1-12. *Changes in the elemental composition (left) and chemical states of Cu (right) during depth profiling of the stainless steel brush-cleaned sample Pos#4N. Note that the sputtering speed is approximately 50 % of the sputtering speeds of the other depth profiles.*

Appendix 2

Program listing in Python for colour calculations of the specular reflected light

```
"""Script to calcualte the specular colour and spectra of copper
oxide films
on a copper substrate.

Programmer: Matts Bjorck (Matts.Bjorck@skb.se)
Last changed: 2016-04-03
"""

import numpy as np
import pylab as pl

def refl(theta,lamda,n,d):
    """Calcualte the reflectvity for s-polarised thin films using
the
    parratt algorithm

    Parameters:
        theta - incident angle in degrees
        lamda - wavelength of the light
        n - the refractive index
        d - the thickness of the layers

    Returns:
        R - the reflectivity
    """
    d=d[1:-1]
    # Length of k-vector in vaccum
    k=2*np.pi/lamda[np.newaxis, :]
    Qj=2*n[-1][np.newaxis, :]*k*np.sqrt(n**2/n[-1][np.newaxis, :]**2
-
                                        np.cos(theta[np.newaxis, :]*
                                               np.pi/180)**2)
    # Fresnel reflectivity for the interfaces
    rp=(Qj[1:]-Qj[:-1])/(Qj[1:]+Qj[:-1])
    p=np.exp(1.0j*d[:,np.newaxis]*Qj[1:-1])
    # Setting up a matrix for the reduce function.
    rpp=np.array(map(lambda x,y:[x,y],rp[1:],p))
    # Paratt's recursion formula
    def formula(rtot,rint):
            return (rint[0]+rtot*rint[1])/(1+rtot*rint[0]*rint[1])
    r=reduce(formula,rpp,rp[0])
    # return the reflectivity
    return abs(r)**2

def g_corr(l):
    """Correct colour for the gamma value of the display"""
    if l < 0.0031308:
            return 12.92*l
    else:
            return 1.055*l**(1/2.4) - 0.055

def xyz2srgb(X, Y, Z):
    """Transform the XYZ colour coordinates to SRGB"""
    M = np.mat([[3.2406, -1.5372, -0.4986], [-0.9689, 1.8758,
0.0415], [0.0557, -0.2040, 1.0570]])
```

```
    RGB = M*np.mat([X, Y, Z]).transpose()
    return RGB[0,0], RGB[1,0], RGB[2,0]

def spectra2rgb(l, spectra, brightness=4):
    """Transform a spectra (intensity as a function of wavelength
    to a RGB colour
    """
    Pi_tab = np.loadtxt('stand_ill_D65.txt')*1.0
    col_obs_tab = np.loadtxt('col_obs_1931.txt')*1.0

    Xl = np.interp(l, col_obs_tab[:,0], col_obs_tab[:,1])
    Yl = np.interp(l, col_obs_tab[:,0], col_obs_tab[:,2])
    Zl = np.interp(l, col_obs_tab[:,0], col_obs_tab[:,3])

    Pil = np.interp(l, Pi_tab[:,0], Pi_tab[:,1])
    Pil = Pil/np.trapz(Pil, x=l)*brightness

    X = np.trapz(Pil*Xl*spectra, x=l)
    Y = np.trapz(Pil*Yl*spectra, x=l)
    Z = np.trapz(Pil*Zl*spectra, x=l)
    R, G, B = xyz2srgb(X, Y, Z)
    print 'Raw RGB:', R, G, B
    R = np.clip(g_corr(R), 0, 1)
    G = np.clip(g_corr(G), 0, 1)
    B = np.clip(g_corr(B), 0, 1)
    print 'Clipped RGB: ', R, G, B

    return R, G, B

if __name__ == '__main__':
    # Flags for the different simulations
    example_spectra = True
    colour_squares = True
    # Create the wavelength array
    l = np.arange(300, 1100, 1)
    # The incident angle
    theta = 90*np.ones_like(l)
    # Loading the refractive indices
    Cu_tab = np.loadtxt('Cu_palik.nk', comments=';')
    CuO_tab = np.loadtxt('CuO_palik.nk', comments=';')
    Cu2O_tab = np.loadtxt('Cu2O_palik.nk', comments=';')

    n_Cu = (np.interp(l, Cu_tab[:,0]/10., Cu_tab[:,1]) +
                        1.0J*np.interp(l, Cu_tab[:,0]/10.,
Cu_tab[:,2]))
    n_CuO = (np.interp(l, CuO_tab[:,0]/10., CuO_tab[:,1]) +
                         1.0J*np.interp(l, CuO_tab[:,0]/10.,
CuO_tab[:,2]))
    n_Cu2O = (np.interp(l, Cu2O_tab[:,0]/10., Cu2O_tab[:,1]) +
                          1.0J*np.interp(l, Cu2O_tab[:,0]/10.,
Cu2O_tab[:,2]))

    if colour_squares:
        # Plot colour squares in a row
        brightness = 5
        thick_levels = 6.
        thick_max = 25.
        thick = np.linspace(0, thick_max, thick_levels)
        color_im = np.zeros((thick.shape[0], 3))
        n = np.c_[n_Cu, n_Cu2O, n_Cu*0 + 1].transpose()
        pl.figure()
```

```
        pl.gcf().clf()
        R, G, B = spectra2rgb(l, np.ones_like(l), brightness)
        axes = pl.subplot(1, thick_levels + 1, 1, axisbg=(R,G,B),
                                  aspect='equal')
        pl.title('White')
        axes.get_xaxis().set_visible(False)
        axes.get_yaxis().set_visible(False)
        for i, d_ox in enumerate(thick):
            d = np.array([0.0, d_ox, 0.0])
            r = refl(theta, l, n, d)
            R, G, B = spectra2rgb(l, r, brightness)
            print R, G, B
            color_im[i,0] = R
            color_im[i,1] = G
            color_im[i,2] = B
            axes = pl.subplot(1, thick_levels + 1, i + 2,
axisbg=(R,G,B),
                                  aspect='equal')
            pl.title('%d nm'%d_ox)
            axes.get_xaxis().set_visible(False)
            axes.get_yaxis().set_visible(False)
        pl.show()

    if example_spectra:
        # Calculate spectra for a Cu surface:
        n = np.c_[n_Cu, n_Cu*0 + 1].transpose()
        d = np.array([0.0, 0.0])
        r_cu = refl(theta, l, n, d)

        # Calculate spectra for a Cu/Cu2O 10 nm film:
        n = np.c_[n_Cu, n_Cu2O, n_Cu*0 + 1].transpose()
        d = np.array([0.0, 10.0, 0.0])
        r_ox = refl(theta, l, n, d)

        np.savetxt('Example_spectra.dat', np.c_[l, r_cu, r_ox])
```

Appendix 3

Comments on the authors' participation

Matts Björck: Responsible for experimental planning, data analysis and report compilation.

Henri Pehkonen: Responsible for the design and construction of the gas shield.

Leena Vuori, Kimmo Lahtonen and Mika Valden: Participated in and conducted the cleaning experiments and XPS experiments and analysis.

Mikael Tigerström: Experimental planning and setup for welding. Responsible for rebuilding the FSW machine.

Lars Cederqvist: Responsible for welding.

Tero Purhonen: Experimental planning for the cleaning experiments, participating in welding experiments and overall planning.

Arkitektkopia AB, Bromma, 2017

A CO-OPERATION REPORT BETWEEN SVENSK KÄRNBRÄNSLEHANTERING AB AND POSIVA OY

SKB's and Posiva's programmes both aim at the disposal of spent nuclear fuel based on the KBS-3 concept. Formal cooperation between the companies has been in effect since 2001. In 2014 the companies agreed on extended cooperation where SKB and Posiva share the vision "Operating optimised facilities in 2030". To further enhance the cooperation, Posiva and SKB started a series of joint reports in 2016, which includes this report.